FINAL REPORT

For

Proof-of-Concept Technology Development Proposal for the Alpha Foundation for the Improvement of Mine Safety and Health AFC518

Grant Number: AFC518-16

Title of Project: Development of a direct sensing sampler for submicron mining particles including coal, silica and nano-sized diesel particulates

Project Period: 09/01/2017–02/28/2019

Awarded Organization: **Colorado State University**

Principle Investigator: **Dr. Su-Jung (Candace) Tsai**
    Contact Information:
    Position/Title: **Assistant Professor**
    Organization Name: **Colorado State University**
    Department: **Environmental & Radiological Health Sciences**
    Mailing Address: **1681 Campus Delivery**
                 Fort Collins, CO 80523-1681
    Phone: **970-491-1340**
    PI Email: **candace.tsai@colostate.edu**

Acknowledgement/Disclaimer:

Table of Contents

2.0 Executive Summary

Technology Concept: Submicrometer- and nanometer-sized particles are a potentially severe but largely unstudied exposure in the mining environment. Workers in the mining environment might be exposed to high amounts of nanometer-sized particles from coal dust, silica particles and diesel exhaust, but currently available respirable sampling methods are unable to quantify this exposure.

Proof-of-Concept Methodology: The goal of this project is to meet the performance requirements of a personal sampler that can measure the nanometer and submicrometer portion of respirable particles. A sampler was designed to collect particles within the respirable size range without using a cyclone as a pre-separator, and a direct reading capacitive sensor was designed to measure the deposited particles in real time. These new features are not available from currently used samplers and direct-reading instruments. The capacitive sensor strip attached to the filter in the sampler enables real-time monitoring of deposited particles within the range of particle sizes selected by the inlet nozzle design and air flow of the sampler. This sensing approach relies on a shift in capacitance due to the dielectric loading of particles deposited on the interdigitated capacitor structure. A grid-attached filter is used to collect particles in the nanometer to micrometer size range; deposited particles can then be analyzed through both real time measurement and offline analysis. Particle size distribution can be determined from offline microscopy and image analysis. Particle size, particle quantity and environmental humidity are considered in the design.

Evaluation Outcome: The proof-of-concept device was developed by using a capacitance sensor integrated with a specially designed particle sampler, and the results showed a clear response to particle deposition by the sensor. The particles collected with the designed sampling cassette had a count median diameter (CMD) of 113 nm and a mass median aerodynamic diameter (MMAD) of 1.65 μm for particles collected on the filmed transmission electron microscope grid, and a CMD of 548 nm and MMAD of 3.36 μm for particles collected on the filter operated at a 0.3 L/min flow rate. The sampler provides stable sampling results and is suitable for long-term sampling at high concentrations and does not encounter pressure buildup issues. The capacitance sensor shows a clear response to particles deposited on the sensor, and the positive shift in capacitance is consistent with increased counting by the sensor and the particle number concentration by direct reading real time particle spectrometers. The sensor has demonstrated detection capability for a small portion of particles as well as selectivity for small particles.

Technology Readiness: The sensor detection was successful from low concentrations to concentrations approximately 10 mg/m^3 or higher. This project demonstrated the success of detecting and measuring small particles through a methodology unique among other currently available technologies. The current generation of our technology uses a micro-USB port for power and data transfer to a computer. In the next generation, wireless communication can be applied through Wi-Fi or Bluetooth, and a commercial battery can be used for power. Though we minimized the parasitic capacitance from the substrate, parasitic capacitance remained on the readout and interface printed circuit boards. The fractional change in sensor capacitance is thus not purely reflected in the fractional change in the number of counting, owing to the parasitic capacitance. For instance, although the readout calibration using fixed capacitors estimated a resolution of ~15 fF/count, test results using road dust showed ~42 fF/count. Thus, further development is necessary to maximize the fractional change in the sensor and to minimize parasitic capacitance from the readout and interface boards.

3.0 Concept Formulation and Mission Statement

The mission of this research was to develop and demonstrate the concept of a new personal sampler that can measure workers' exposure to particles in the submicrometer and nanometer size range. On the basis of the currently available technology, no sampling method can determine the quantity or provide the count distribution of submicrometer- and nanometer-sized particles in the mining environment. We used a newer personal sampler model designed by the PI (Figure 1) to develop a sampling device with a real-time sensor to measure particles. We aim to develop this sampling device to monitor the portion of mine dust with particle sizes too small to be measured by using the traditional gravimetric method, owing to their very low mass.

This new sampler utilizes the airflow pattern and geometric design of the sampling cassette to provide more accurate particle size segregation for entering the sampler and then deposit on the two substrates (grid and filter). This design also has a higher efficiency than other samplers for collecting particles. One unique feature is that the design of the sampling cassette inlet serves as a pre-separator for respirable mass, thus eliminating the need for a cyclone; as a result, the sampling device is much easier to wear in the harsh environments encountered by miners.

Rationale for the concept formulation:

This design approach was chosen because it is uniquely capable of meeting the performance requirements of a personal sampler that can measure the nanometer-sized portion of respirable particles in the mining environment from microscopic images of the sampled particles. To our knowledge, no other technology can meet these design goals, including the currently used respirable particle cyclone sampler and the personal dust monitor.

Figure 1

The particle size entering the sampler cassette seen in Figure 1 is determined by a combination of the inlet nozzle size and the sampling air flow. As demonstrated by Su and Vincent (Su and Vincent 2004), the aspiration efficiency of a plain round inlet such as the inlet nozzle at the top of the cassette, as shown in Figure 1, follows a sigmoidal curve similar to the respirable pre-separator curve. The cut diameter (50% cumulative size, D50) of the curve is a function of the inlet diameter and air flow, and must be determined experimentally. The collection is minimally affected by sampling direction (upward, horizontal or downward), as found with our design (Figure 1) and in the study by Su and Vincent (Su and Vincent 2004). Using the cassette inlet nozzle as a pre-separator is also the design principle of the Institute of Medicine (IOM) inhalable mass sampler. Through experimental determination of the proper combination of inlet diameter and air flow, the aspiration efficiency of the sampling cassette closely matches the American Conference of Governmental Industrial Hygienists (ACGIH) inhalable mass sampling criterion.
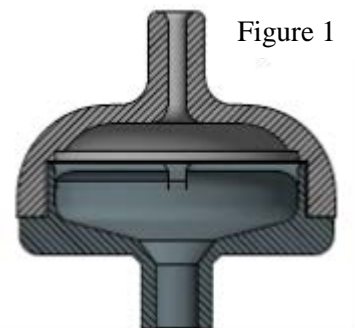
The theory on collecting more small particles on the filmed-grid is based on Brownian motion and diffusion when small particles flow past the surface of, but not through, the grid. Particles larger than the pore diameter (200 nm) are collected with 100% efficiency on the filter surface, while particles smaller than the pore diameter are collected with high efficiency by impaction, interception and Brownian motion when the air flows through the pores. The particle collection method used here is not affected by gravity, and it yields the same results for any physical orientation, e.g., when workers are in moving, bending or

crawling positions. Because it uses a 25 mm filter cassette and no cyclone pre-separator, this sampler, together with the electrical sensor, is small and lightweight for personal sampling and can be mounted at the worker's breathing zone.

The current personal dust monitor (PDM3700) for mining dust uses tapered-element oscillating microbalances (2000). Our device utilizes a capacitance approach, which is more easily integrated on the inlet side of the filter, and which can be replaced daily along with the filter membrane (Health 2010). The basic readout approach for the capacitive sensor is comparable to that in TEOM monitors (Rupprecht, Meyer et al. 1992, Chan and Y.S. 1999, 2000, Cyrysa, Dietrich et al. 2001, Charron, Harrison et al. 2004); i.e., a change in the deposited thickness of particle layer is directly and sensitively read through a shift in resonance frequency. In this case, the resonance is in an electrical circuit (inductor-capacitor) rather than mechanical vibration. To minimize effects of humidity and water droplets, the temperature of the membrane could be maintained at approximately 100 °C, through use of an electrical (resistive) heater incorporated on the housing and resistive thermometers incorporated on the capacitive sensor strip.

Mission Statement:

We designed a sampling device utilizing a capacitance sensor to enable real-time detection of dust exposure. The capacitance-based approach allows for real-time detection of incremental and total particle deposition on the filter. Its features include 1) direct collection of submicrometer and nanometer-sized particles, 2) direct reading of the mass concentration of collected particles, 3) offline analysis of the number, concentration and size distribution of collected particles, 4) effective sampling in all orientations, 5) a lack of influence of ambient temperature and humidity, 6) measurement of actual mass as an alternative to direct-reading measurements and 7) safety and ease of use in the mining environment. These features overcome the drawbacks of currently available sampling techniques.

To achieve the goal, our research objectives included: 1) constructing a prototype personal sampler through 3D printing, 2) assembling the electrical sensor with the personal sampler, 3) optimizing the geometry of the sampler and 4) testing the sensor function and the correlation to the quantity of sampled particles.

According to the objectives, we performed the tasks listed below:

Task 1: Print the sampler cassette by using a 3D printer with two printing materials: polystyrene and nylon.
Task 2: Test samplers on the inlet pre-separator efficiency and collection efficiency of the substrate (grid and filter).
Task 3: Design the sensor and assemble on the sampler cassette.
Task 4: Test the electrical sensitivity.
Task 5: Test the assembled sampler through dust collection.
Task 6: Adjust the geometry of the sampler as necessary to optimize sampling.
Task 7: Correlate the electrical signal to the weighed mass and analyzed particle concentration by using transmission electron microscopy (TEM).
Task 8: Convert the electrical signal from mass to a direct reading of mass concentration.
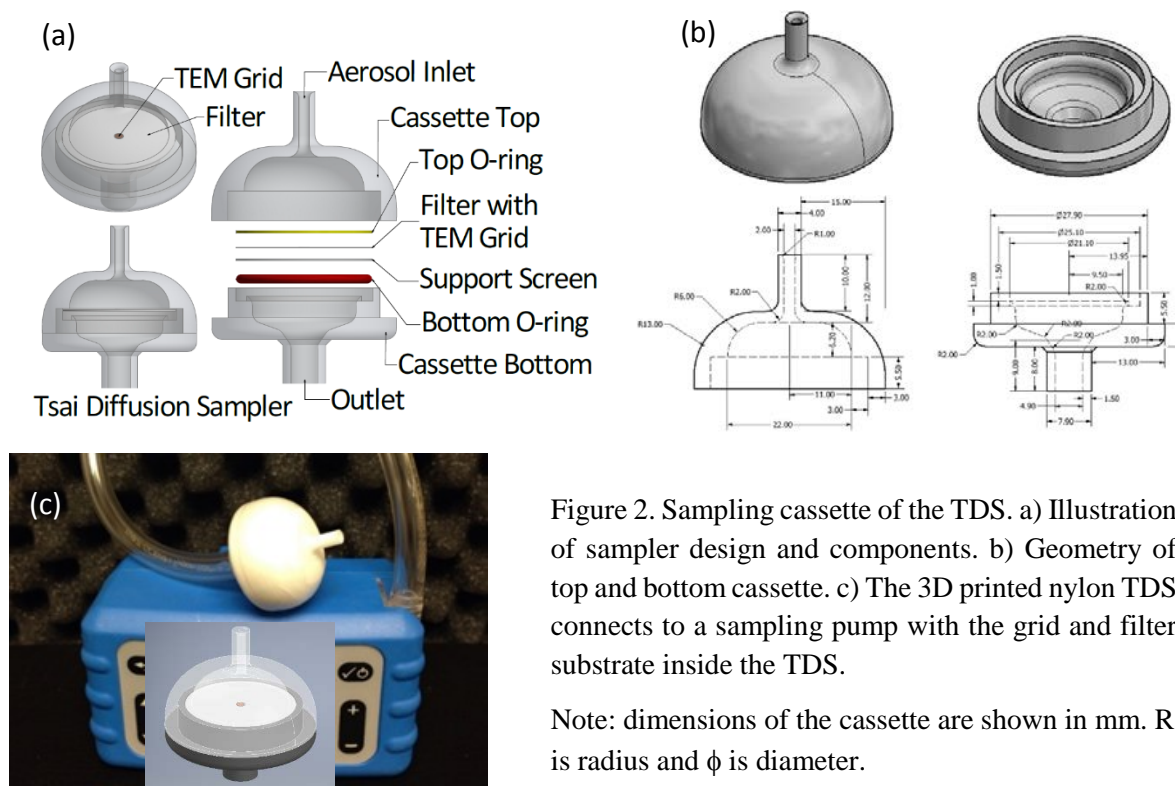
4.0 Proof-of-Concept Technology Components

4.1 Sampling cassette

The sampling cassette has been designed, and a patent has been filed. The cassette was named the Tsai diffusion sampler (TDS) and is shown in Figure 2a. The design was published in 2018 (Tsai and Theisen 2018). This TDS collects particles in the nanometer and respirable size ranges with an aerodynamic cutoff diameter (D50) of approximately 3.8 µm, as determined experimentally, for respirable particles.

The novel geometry design of the TDS includes 1) a 2 mm diameter circular-bell shape air inlet with a nozzle length of 10 mm, 2) a 6 mm distance between the grid substrate and the inlet opening at the top of a 25 mm diameter cassette housing (which meets the recommended design criterion of Hinds (Hinds 1999)) and 3) a smooth curved shape of the top cassette housing, to provide smooth, streamlined air flow to move particles from the inlet toward the sampling substrate filter and grid. The dimensions of the geometry design are shown in Figure 2b. Together with the air flow, these factors determine the sizes of particles entering the cassette and thus the cutoff diameter of the particles collected on the two substrates. The TDS substrates consist of a 25 mm diameter, 0.22 µm pore size polycarbonate membrane filter (Isopure, Millipore Sigma, Burlington, MA, USA) with a 400 mesh TEM-copper grid with SiO_2 coated film (SPI, West Chester, PA, USA) attached to the center of the filter (Figure 2a and 2c). The polycarbonate membrane filter enables analysis of collected particles on the filter through scanning electron microcopy (SEM). It is operated with a personal sampling pump running at 0.3 L/min air flow (Figure 2c), pulling particles in the air through the 2 mm diameter circular inlet into the cassette housing. Particles are then collected on both the grid and filter (Figure 2a and 2c).

The cassette was designed in Autodesk Inventor 2018 and was 3D printed (ProX 500, 3D Systems, Rock Hill, SC, USA) through selective laser sintering (SLS) of nylon powder (DuraForm ProX PA, nylon 12- CAS: 25038-74-8). SLS is often used in rapid manufacturing practices, and its utility has been demonstrated in the automotive and aerospace industries (Zarringhalam, Hopkinson et al. 2006). The ProX 500 system used here is able to efficiently manufacture ready to use functioning parts with high resolution and dimensional accuracy (Systems 2017).

Figure 2. Sampling cassette of the TDS. a) Illustration of sampler design and components. b) Geometry of top and bottom cassette. c) The 3D printed nylon TDS connects to a sampling pump with the grid and filter substrate inside the TDS.

Note: dimensions of the cassette are shown in mm. R is radius and ϕ is diameter.

4.2 Sensor components (sensor and heater)

The capacitance-based sensor works on the basis of a capacitance shift due to particle deposition. The interdigitated patterns provide higher sensitivity in a given area where electrodes with different polarities are interchanged. The entire size of the sensor was determined such that it minimizes the air flow interference and facilitates easy connection with the readout board when integrated with a TDS. Thus, the sensor strip has a rectangular shape with dimensions of 2 mm × 20 mm, as shown in Figure 3a. The sensor is located at one end of the strip, and the actual sensing area is 1 mm × 1.5 mm. The sensor strip also includes an integrated resistance-based microheater suitable for holding the sensor at a controlled elevated temperature; this capability provides a means to mitigate the effects of condensation/water droplets and enhances the stability of the capacitance. In addition, it reduces the complexity of installing a heater inside the sampler, avoiding extra interfaces for heaters. Sensors were made through microfabrication technologies as follows: 1) sensor and microheater patterning by photolithography, 2) metallization of substrate by using aluminum and 3) lift-off of metals by photoresist removal. Figure 3b shows the sensors fabricated on polyimide substrate. The flexible sensor/heater strips were batch-fabricated through scalable microfabrication approaches.

To facilitate integration with the modified TDS and readout board, the sensor/heater strips were mounted on an interface printed circuit board (PCB), as illustrated in Figure 4a. The interface PCB enables robust electrical and mechanical connections to the main readout board, via the pin connections shown at
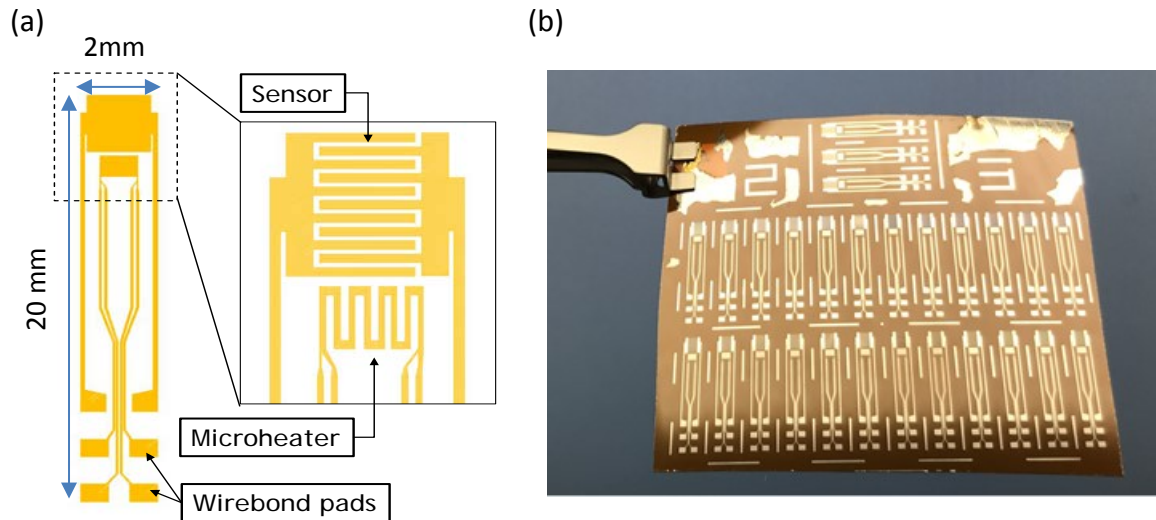
Figure 3. a) Layout of capacitance-based sensor/heater strip and b) array of 24 strips fabricated on Kapton substrate by using scalable micro-fabrication approaches.

the bottom of Figure 4a. As shown in Figures 4b and 4c, the assembly is then mounted to a modified TSD device for particle monitoring. A simulation study using a computational fluid dynamic program shows that particle distribution inside the TDS depends on the particle size, as shown in Figure 5. Whereas particles smaller than 3 μm are uniformly distributed over the filter area, particles larger than 3 μm are preferentially located in the center area. To avoid contributions from large particles, the sensor is located approximately 4 mm away from the center. Like batch-fabricated sensor strips, low-cost interface PCBs can be disposed of with sensors as needed.
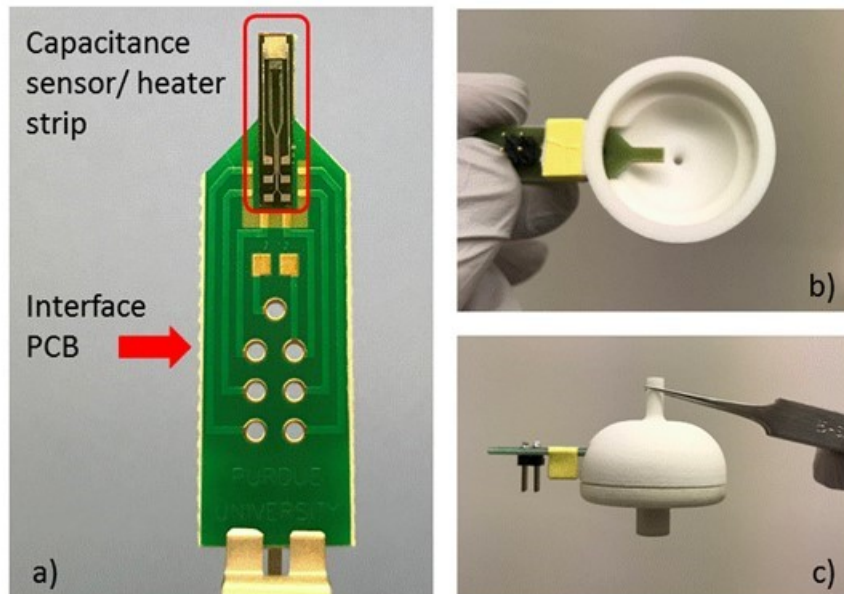

Figure 4. Photographs of a) capacitance sensor/heater strip mounted on interface PCB; and b) and c) strip/interface PCB assembly mounted in a modified TDS, showing bottom and side views, respectively.

In addition to testing with laboratory capacitance meters, we have developed an integrated readout approach using a microcontroller mounted on a custom designed PCB (Figure 6). The integrated readout

approach measures the time constant of an electrical circuit consisting of the capacitance sensor and an external resistor. As the capacitance of the sensor increases due to particle deposition, the corresponding increase in the time constant of the resistance-capacitance circuit is converted into a shift in counts in a sampling circuit, realized by using the microcontroller. Data from the microcontroller can be downloaded through a USB port or over Wi-Fi.
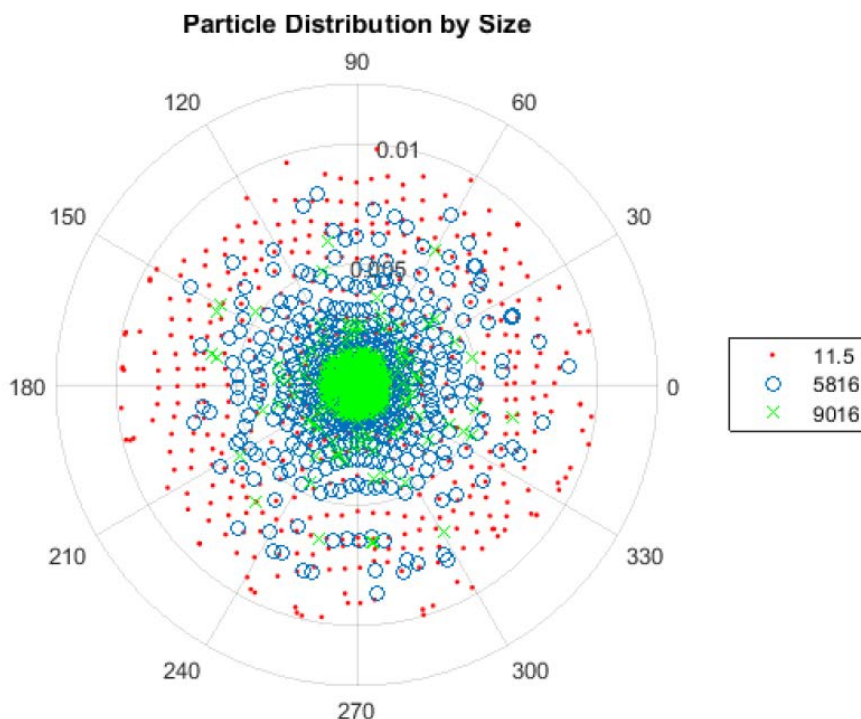

Figure 5. Radial particle distribution by size. Small dots (red) represent particles with 11.5 nm diameter, circles (blue) represent particles with 5.8 μm, and crosses (green) represent particles with 9.0 μm.
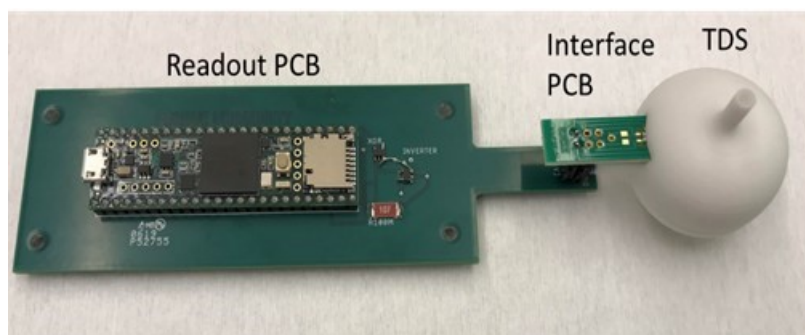

Figure 6. Assembly of a micro-controller based readout circuit (large PCB on left), capacitive sensor board and Tsai sampler housing (right). Electrical connections between the two boards allow for easy replacement of the capacitive sensor board, e.g., at the start of a work shift.

5.0 Proof-of-Concept Evaluation

5.1 Methods

5.1.1 Cassette sampling to determine sizes of respirable and nanoparticles

We generated aerosol to perform efficiency testing and evaluated the cutoff diameter of the collected particles. Three types of aerosol were used for the initial trial test: sodium chloride particles, road dust and aluminum oxide. Crystalline aluminum oxide (Al_2O_3) nanopowder (Nanodur, Nanophase, Romeoville IL, USA), with a density of 3600 kg/m^3 and a primary particle size of 40 nm, was found to be a suitable aerosol to determine the particle size distribution of the collected particles in the TDS. This nanopowder was chosen because of the wide range of aerosol particle sizes from individual primary particles to small and large agglomerates, and the ease of aerosolizing the particles. Road dust was chosen because it is the fine test dust required for ISO 12103-1 A2 standard test, and it contains 68-76% silica.

The experimental setup is illustrated in Figure 7. To generate aluminum oxide, powder was aerosolized inside an ultra-filtered glove box (Terra Universal, Fullerton CA USA, 89 cm × 61 cm × 64 cm) through agitation by stirring 200 mL of aluminum oxide in a container with a compact digital mixer operating at 2000 rotations per minute (rpm) (Cole-Parmer, Vernon Hills IL, USA). The agitator, powder and sampling cassettes were placed inside the glove box at the center (Figure 7), and the aluminum oxide aerosols were diffused to the top opening of the container and pulled into samplers and instruments. Two direct reading real time instruments (RTIs) were utilized to measure particle number concentrations and size distributions over a range of 10 nm to 10 µm. An optical particle sizer (OPS) (model 3330, TSI, Shoreview, MN, USA) with a measuring range of 0.3 µm to 10 µm and a NanoScan scanning mobility particle sizer (NanoScan SMPS) (model 3910, TSI, Shoreview, MN, USA) with a measuring range of 10 nm to 420 nm collected side by side measurements at 1-min intervals. The RTIs sampled through 1 m of conductive tubing. The RTIs and three identical TDS samplers were positioned equidistant from one another and 5 cm away in both height and distance from the source (Figure 7). The air velocity at the sampling area ranged from 1 to 7.6 cm/s (2 to 15 ft/min) in the horizontal direction and from 0 to 3 cm/s (0 to 6 ft/min) in the vertical direction. The glove box and all experimental equipment were decontaminated with clean room wipes and distilled water before experimentation.
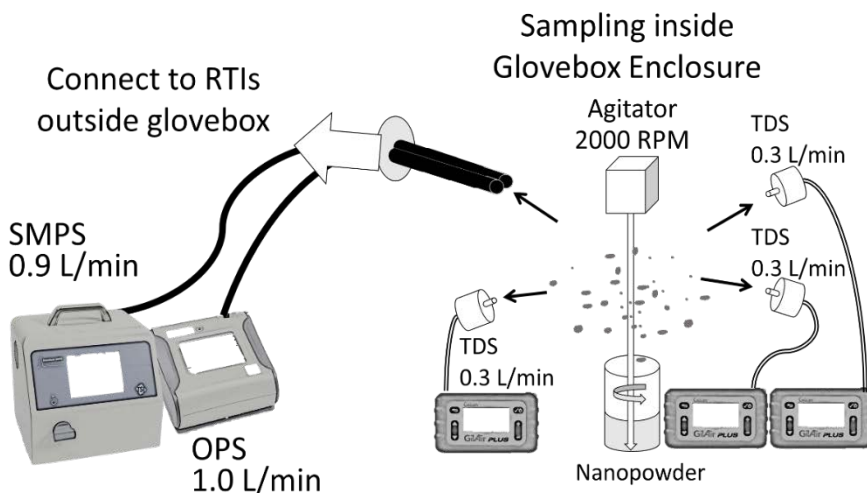

Figure 7. Illustration of experimental setup for laboratory particle sampling.
Note: The RTIs and three identical TDS samplers were positioned equidistant from one another and 5 cm away in both height and distance from the source.

The RTIs initiated sampling 10 min before aerosol generation to establish background concentrations. Immediately after, the three personal sampling pumps and the compact digital mixer were activated. Aerosol generation was conducted for 40 min. After the sampling period, 10 min of post experimental background was measured with the RTIs. The RTI data were exported to an Excel spreadsheet and analyzed. The TDS TEM grid and filter samples were analyzed with TEM (JOEL JEM-2100F) and SEM (JOEL JSL-6500F), respectively. Collected particles were imaged according to the protocols below.

The following TEM imaging protocol was utilized to analyze grids: 1) five low magnification (50×) images were taken to encompass the entire grid (center and four quadrants); 2) four grid spaces were selected equidistant two spaces from the grid center, and these spaces were imaged at 500×; 3) the chosen grid spaces were imaged by traversing (9–12 images per grid) the grid space at 5000× until 300 particles were imaged.

For filter analysis with SEM, the filters were prepared by cutting a 1/8th slice of the filter and coating with 10 nm of gold. Three sections of the filters were imaged (center, middle and edge) at 9000–25000× until 300 particles were imaged per sample. Particle images were analyzed in FIJI (Schindelin, Arganda-Carreras et al. 2012) imaging software to count particles and measure particle size. The particle sizes were organized according to 13 bin ranges within 10 nm to 420 nm and 14 bin ranges above 420 nm to 10 µm, similarly to two RTI bin ranges, to plot particle count frequency with size distribution and cumulative percentage particle counts. We also used statistical program to plot particle counting and sizing data with over 900 particle counts for each set of analysis.

The experimental setup and analysis method was repeated with TDS cassettes operating at 0.3 L/min and 0.9 L/min to examine the effect of operating flow rate on the observed particle collection size distributions. Identical setups and operating conditions were used to examine this relationship.

5.1.2 Technical aspects of sampling

We evaluated the particle collection efficiency of the polycarbonate membrane filter (Isopure, Millipore Sigma, Burlington, MA, USA) used in the TDS. ISO fine test dust (12103-1 A2), referred as road dust, 73% silica with a CMD of 5–11 µm, was used to test TDS. Generation of a road dust aerosol was achieved with a Wright Dust Feeder (WDF II, Westwood NJ, USA) operating at 10 PSI and 1 RPM.

Penetration was measured with three TDS samplers connected in parallel to a NanoScan SMPS (model 3910, TSI, Shoreview, MN, USA), which has a measurement range of 10–420 nm and was operated with a 0.9 L/min flow rate. Adjacent to the TDS and NanoScan SMPS sampling array, a second NanoScan SMPS was positioned 5 cm away and measured the aerosol concentration entering the TDS. By observing the particle counts measured by the second NanoScan SMPS and comparing those values to the NanoScan SMPS measuring downstream of the TDS samplers, we were able to estimate the amount of breakthrough occurring within the TDS sampler equipped with a polycarbonate membrane filter. Three TDS samplers were connected to the first NanoScan SMPS so that the flow rate through each sampler was 0.3 L/min, the operating flow rate of the TDS. The dust feeder was run for a 30 second interval every 30 min during the 4-hour sampling period denoted by the sharp peaks on the total concentration graphs of direct reading RTIs.

5.1.3 Particle loading

To quantify the relationship between particle loading (collected mass) and the pressure drop, we conducted three identical experiments. Three TDS samplers were arranged in a triangular fashion so that the centers of all sampler inlets were 25 mm apart. The array of TDS samplers was positioned 30 cm away

from a Wright Dust Feeder, which generated road dust aerosol within an ultra-filtered glove box. Operating at 0.3 L/min, the TDS samplers collected road dust for a 4-hour sampling period. Plastic Y shaped connecters were used to connect Dwyer Series 475 digital manometers downstream of the sampling cassette before the pump driving the cassette. The polycarbonate membrane filters used inside the TDS samplers were desiccated and weighed before and after the 4-hour sampling period to determine the mass collected.

To further evaluate the sampler's performance during long term sampling, a 16-hour sampling of road dust was conducted to examine the effect of long-term particle loading on the polycarbonate membrane filters utilized by the TDS. The experiment consisted of three sessions including a 4-hour sampling period followed by two 6-hour sampling periods. We created a road dust aerosol by utilizing a Wright Dust Feeder, operating at 10 PSI and 0.5 RPM. The three cassettes and RTIs were positioned equidistant and 15 cm from the aerosol source within an ultra-filtered glove box. Plastic Y shaped connectors allowed Dwyer Series 475 digital manometers to be connected to the Tygon tubing connecting the sampling cassettes to the pumps. This connection allowed for the monitoring of pressure changes for the duration of the experiment. Three different cassettes were used for this experiment: one TDS operating at 0.3 L/min, one open face cassette operating at 0.3 L/min and one open face cassette operating at 2 L/min. The 2 L/min sample enabled examination of the worst-case scenario of an overloaded filter with a substantial mass collected. Small drops in pressure were observed in the pressure drop over sampling time curves that represented the ending of each sampling period when the cassettes were turned off before being restarted the next day for the next sampling period.

5.1.4 Cassette material evaluation

We examined the effect of the difference in cassette material (nylon and polystyrene) on overall particle collection. Two cassette materials were examined for this study: nylon and high impact polystyrene (HIPS). Comparing the collected mass for paired samples allowed us to examine the performance of the cassette material. An aerosol of road dust was generated with a Wright Dust Feeder, operated at 10 PSI and 0.5 RPM into an ultra-filtered glove box. Cassettes were paired, with one nylon and one polystyrene, so that the centers of the inlets were 25 mm apart and were positioned identically within the glove box. A 1-hour sample was collected for each cassette operating at 0.3 L/min. Filters were desiccated and weighed both before and after the experiment to determine the overall mass collected.

5.1.5 Sensor component test

The sensor and readout board were calibrated before testing. The readout circuit monitors the sensor response by reading the shift in counts as a result of changes in the resistance-capacitance time constant. To confirm the capability of sensor reading, we used fixed capacitors with different capacitance values, as shown in Figure 8. Because the readout board itself had parasitic capacitance, the initial counting did not begin from zero. The results showed that counting increased linearly with increasing capacitance. After calibration with the fixed capacitors, the actual capacitive sensors were compared. The counting of two different sensors matched well with this linear curve. Of note, the capacitance values were measured with a tabletop capacitance meter with an accuracy of ± 0.02 picofarad (pF).
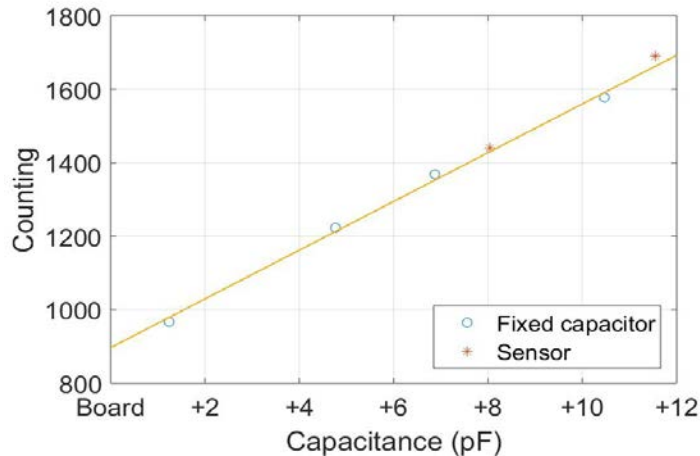
Figure 8.
Readout board counting with respect to capacitance change. The calibrated line was made by using fixed capacitors and compared with actual sensors.

5.1.6 Assembly and evaluation of cassettes and sensors

The top portion of the TDS cassette was modified so that the sensor could be inserted into the cassette flush with the filter surface. The modification (Figure 9) includes a 20 mm long stand to support the sensor and an opening 2.5 mm high and 10 mm wide. After placement of the sensor, the opening was sealed using paraffin wax.

Sensor readout was examined through several experiments utilizing road dust. Two TDS cassettes, one with a sensor and one standard (without sensor), were positioned 10 cm away from the road dust generation source. Generation of road dust aerosol was achieved with a Wright Dust Feeder operating at 10 PSI and 1 RPM. The dust feeder was run for 30 second intervals every 30 min during particle generation. RTIs were positioned 5 cm away from the TDS samplers.

The capacitance sensing approach was demonstrated with road dust, with the capacitance sensor mounted in a TDS (as shown in Figure 4). To facilitate sensor testing at Purdue University, we made a custom-designed acrylic chamber (20 cm × 20 cm × 20 cm). Figure 10 shows the schematic of the test setup with a modified TDS. The assembled modified sampler was installed on the side wall of the chamber, and the inlet of the TDS was inserted through an opening. The outlet of the sampler was connected to an air pump for constant air flow (0.3 L/min), and the road dust was sprayed periodically from the top side of the chamber. The readout PCB was connected to a computer via a USB port for real-time sensor monitoring.
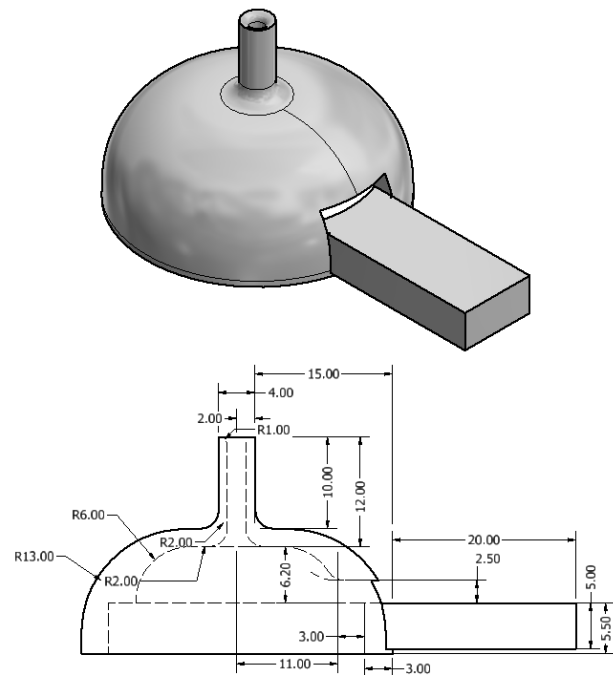

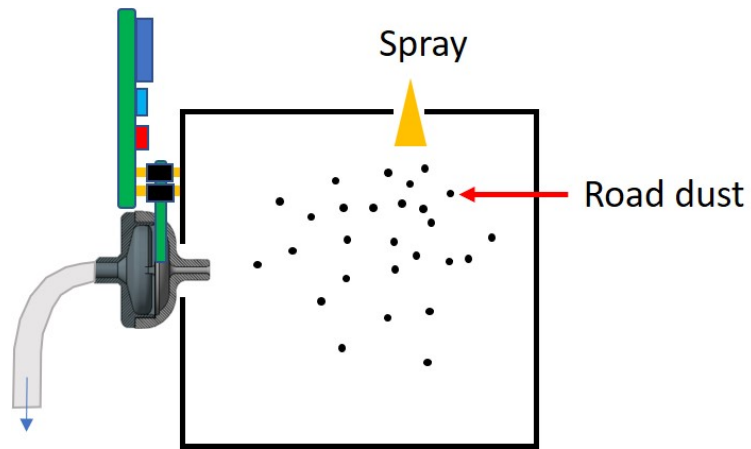Figure 9. Modified TDS cassette top piece to fit the sensor and readout board.

Figure 10. Schematic of the test setup with modified TSD.

5.2 Results of sampling cassette (TDS) performance

5.2.1 Particle collection by TDS

We evaluated particle deposition on the collecting substrates, filter and grid, in the sampling cassette-TDS before the sensor was installed. The variables anticipated to affect the sizes and size distribution of collected particles included the sampling air flow rates, i.e., 0.3 L/min and 0.9 L/min, and the materials, i.e., nylon and polystyrene, used for making the cassette.

To evaluate the effect of sampling flow rate, we compared the cutoff size (D50) and size distribution of the collected particles. The D50 size was determined experimentally with aluminum oxide engineered nanoparticles for 0.3 L/min and 0.9 L/min flow rates. Approximately 900 particles collected on the TEM grid or filter were measured on the basis of their equivalent diameters relative to spherical particles. The data shown in Table 1 were calculated on the basis of approximately 900 particles. At a 0.3 L/min flow rate, particles collected on the TEM grid samples resulted in a CMD of 112.84 nm with a geometric standard deviation (GSD) of 2.28, as shown in Table 1. Particles collected on the filter samples at a 0.3 L/min sampling flow rate were determined to have a CMD of 548.16 nm with a GSD of 1.87. At a 0.9 L/min flow rate, particles collected on the TEM grid samples resulted in a CMD of 187.11 nm with a GSD of 1.96. The particles on filter samples for a 0.9 L/min flow rate had a CMD of 497.64 nm with a GSD of 2.44. The particles' cumulative distributions are shown in Figure 11.

Table 1. Particle sizes collected on the grid and filter at 0.3 L/min and 0.9 L/min.

Collected Substrate and Flow Rate		Count Median Diameter CMD (nm)	Geometric Standard Deviation GSD	Mass Median Diameter MMD (nm)	Mass Median Aerodynamic Diameter MMAD (nm)
TEM grid	0.3 L/min	113	2.28	872	1650
	0.9 L/min	187	1.96	734	1390
Filter	0.3 L/min	548	1.87	1770	3360
	0.9 L/min	498	2.44	5390	10200

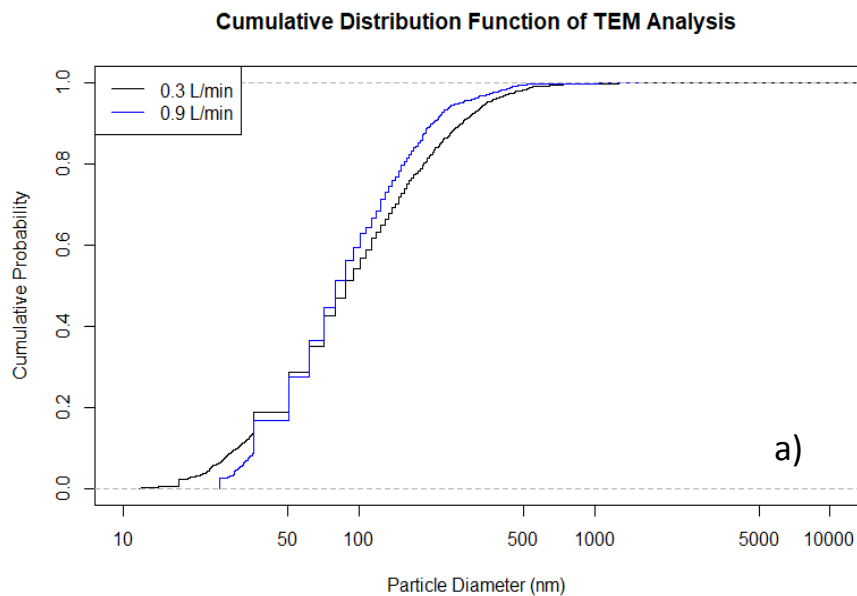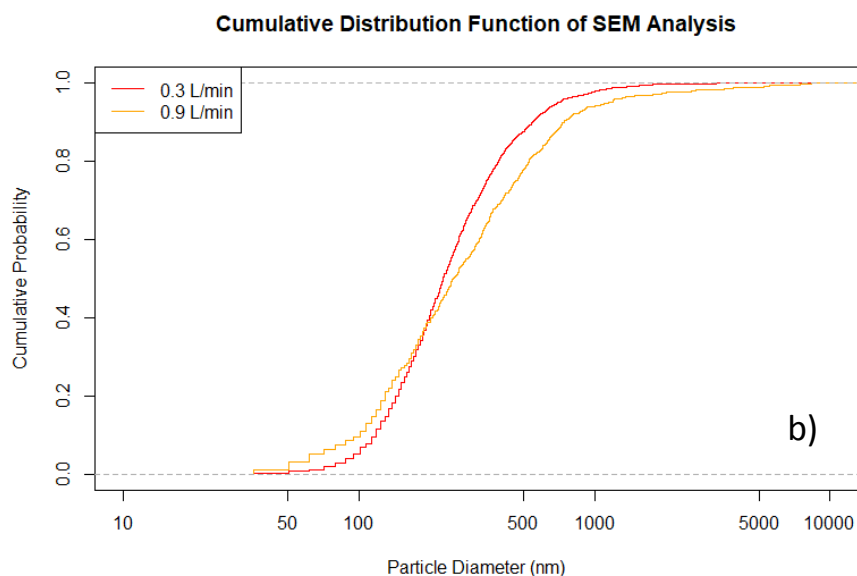## Cumulative Distribution Function of TEM Analysis

Figure 11. Cumulative probability of particle counts and sizes obtained from image analysis of collected aluminum oxide nanoparticles under two operating flow rates: a) particles collected on TEM grids analyzed using TEM; b) particles collected on filter analyzed using SEM.

Note. Each data curve was plotted from more than 900 counts of particles.

On the basis of the data shown in Figure 11, we performed statistical analysis on the CMD of each data set to determine the significance of the effect of operating flow rate. A two-sample Kolmogorov-Smirnov (KS) test was conducted for particles collected on the grid and filter and analyzed by TEM and SEM, to determine whether the flow rates (0.3 L/min vs. 0.9 L/min) influenced the size distribution of the particles analyzed. The KS test is a non-parametric tool that is sensitive to differences in the locations and shapes of the empirical cumulative distribution functions being compared. Comparing the two distributions of particles on TEM grids of the 0.3 L/min and 0.9 L/min flow rates with a KS test led us to conclude that the two distributions were different (D = 0.079191, p-value = 0.002427). KS evaluation of the two distributions of particles on filters of the 0.3 L/min and 0.9 L/min flow rates analyzed by SEM provided further evidence that the two distributions were different (D = 0.11988, p-value = 4.284e-08). The test statistic, D, is the

absolute maximum distance between the cumulative distributions of the samples. The KS test is sensitive to the center of the distribution; therefore, this comparison was repeated with the Anderson-Darling k-sample test (AD). The AD test is weighted to consider the extremes of the distributions (tails). The AD test provided further evidence that the two distributions for both TEM samples (AD = 9.489, p-value = 1.938e-05) and SEM samples (AD = 22.06, p-value = 2.433e-12) were more different than the KS test. The statistical analysis results are summarized in Table 2.

Table 2. Statistical analysis of difference between operating flow rate.

Two-sample Kolmogorov-Smirnov Test	Test Statistic (D)	P-value
TEM	0.079	2.43E-03
SEM	0.120	4.28E-08
Anderson-Darling k-sample Test	Test Statistic (AD)	P-value
TEM	9.49	1.94E-05
SEM	22.1	2.43E-12

It was evident that the operating flow rates, i.e., 0.3 L/min and 0.9 L/min, resulted in significantly different sizes and distributions of the particles collected on the sampling substrates of TDS. However, the CMD and GSD of particles collected on filters at 0.9 L/min showed a much higher GSD than the 0.3 L/min operations, indicating higher variation, a wider range of particle sizes and a larger CMD, results inconsistent with the theory of aerosol science. Although the particles collected on TEM grids indicated that 0.9 L/min operation was consistent with aerosol science theory, providing a narrower size distribution and smaller GSD, and resulting in a smaller CMD, MMD and MMAD than the 0.3 L/min operation (1.7 μm vs. 1.4 μm of MMAD), the particle distribution on the filter showed an unexpectedly wide range and variation indicating the instability of operation at the 0.9 L/min.

For operation at 0.3 L/min, the data analysis results were similar to the results from our previous test. The GSD was very similar, although the MMAD of approximately 3.4 μm was slightly smaller than the previous result of 3.8 μm; thus, we concluded that this operating flow rate was the optimal condition and provides stable sampling results.

5.2.2 Cassette material evaluation

Regarding the effects of the cassette materials, nylon and polystyrene, the dust mass collected on the filters by using two different cassettes and the estimated mass concentrations are presented in Table 3. In six sets of experiments, there was no observed difference for sampling particles between these two materials.

Table 3. Mass concentrations of dust collected by using nylon and polystyrene cassettes

Set	Nylon Cassette Filter Weight (mg)	Nylon Cassette Equivalent Mass Concentration (mg/m^3)	Polystyrene Cassette Filter Weight (mg)	Polystyrene Cassette Equivalent Mass Concentration (mg/m^3)	Mass Difference (mg)
1	0.115	6.39	0.102	5.67	0.013
2	0.027	1.50	0.038	2.11	-0.011
3	0.101	5.61	0.073	4.06	0.028
4	0.034	1.89	0.030	1.67	0.004
5	0.064	3.56	0.075	4.17	-0.011
6	0.023	1.28	0.004	0.22	0.019

5.2.3 Penetration and pressure drop of TDS

Particles smaller than 200 nm may penetrate through the pores (approximately 200 nm diameter) of polycarbonate filters. The results of three experiments, as shown in Figure 12 and Table 4, showed an average breakthrough from 12.31% to 23.84% among all the bin sizes measured with the NanoScan SMPS ranges. Among each size bin, the percentage penetration ranged from 8.54% for the 11.5 nm bin to 20.09% for the 115.5 bin. Two out of three experiments showed much lower penetration, and the one set showing higher penetration may have been attributable to minor leakage. We concluded that the penetration percentage for particles smaller than 200 nm was approximately 15% or lower.

The particle concentrations of generated aerosols in penetration and pressure drop tests are shown in the Appendix. Figures A2, A4 and A6 show the total particle number concentration graphs for each experiment, and Figures A3, A5 and A7 show size-fractionated particle number concentrations.
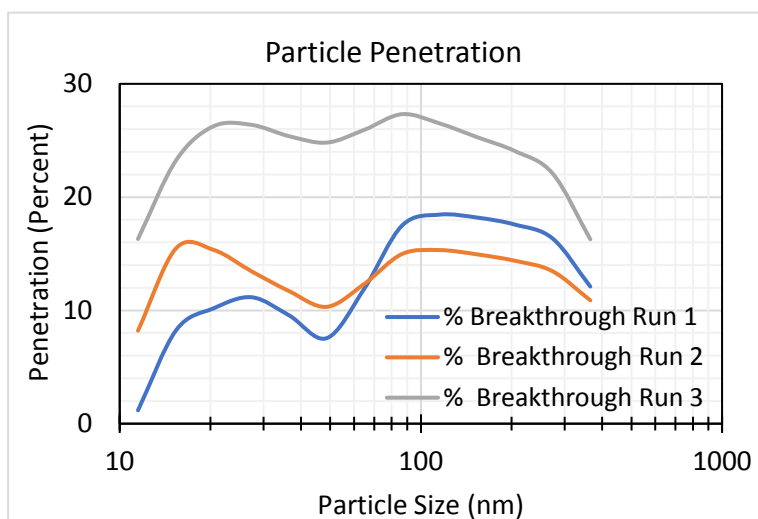

Figure 12. Particle penetration percentage in the size range less than 420 nm.

Table 4. Size-fractioned penetration results

Particle Size Bin Midpoint (nm)	% Penetration Run 1	% Penetration Run 2	% Penetration Run 3	Average Penetration by Bin Size	Standard Deviation
11.5	1.18	8.21	16.3	8.6	6.2
15.4	8.26	15.5	23.3	15.7	6.1
20.5	10.2	15.3	26.3	17.3	6.7
27.4	11.2	13.5	26.4	17.0	6.7
36.5	9.56	11.7	25.4	15.6	7.0
48.7	7.55	10.3	24.8	14.2	7.6
64.9	11.9	12.3	25.9	16.7	6.5
86.6	17.5	15.0	27.3	19.9	5.3
116	18.5	15.3	26.5	20.1	4.7
154	18.2	14.9	25.3	19.5	4.3
205	17.6	14.4	24.1	18.7	4.0
274	16.4	13.5	22.1	17.3	3.6
365	12.1	10.9	16.3	13.1	2.3
Average Penetration by Run	12.3	13.1	23.8		5.3

The pressure at the filter built up during sampling, as expected. The total pressure change and collected dust mass at the end of each sampling experiment are summarized in Table 5. The pressure change profiles throughout the sampling times are included in Appendix Figures A8 to A10. The relationship between collected dust on the filter and the buildup pressure drop is presented in Figure 13.

Table 5. Pressure drop and collected mass at the sampling filter.

	Sample Source	Sample Mass (mg)	Pressure Drop (in H_2O)
Run 1	Manometer 1	0.237	2.77
Run 1	Manometer 2	0.839	1.76*
Run 1	Manometer 3	0.463	2.92
Run 2	Manometer 1	0.178	1.27
Run 2	Manometer 2	0.315	2.17
Run 2	Manometer 3	0.195	1.98
Run 3	Manometer 1	0.142	0.93
Run 3	Manometer 2	0.104	1.50
Run 3	Manometer 3	0.093	0.32

* This measurement is considered invalid.

5.2.4 Particle loading

The collected mass of each sample during penetration tests was also analyzed for particle loading versus sampling time and pressure change, as seen in Figure 13. The pressure change was found to increase as particle loading increased.
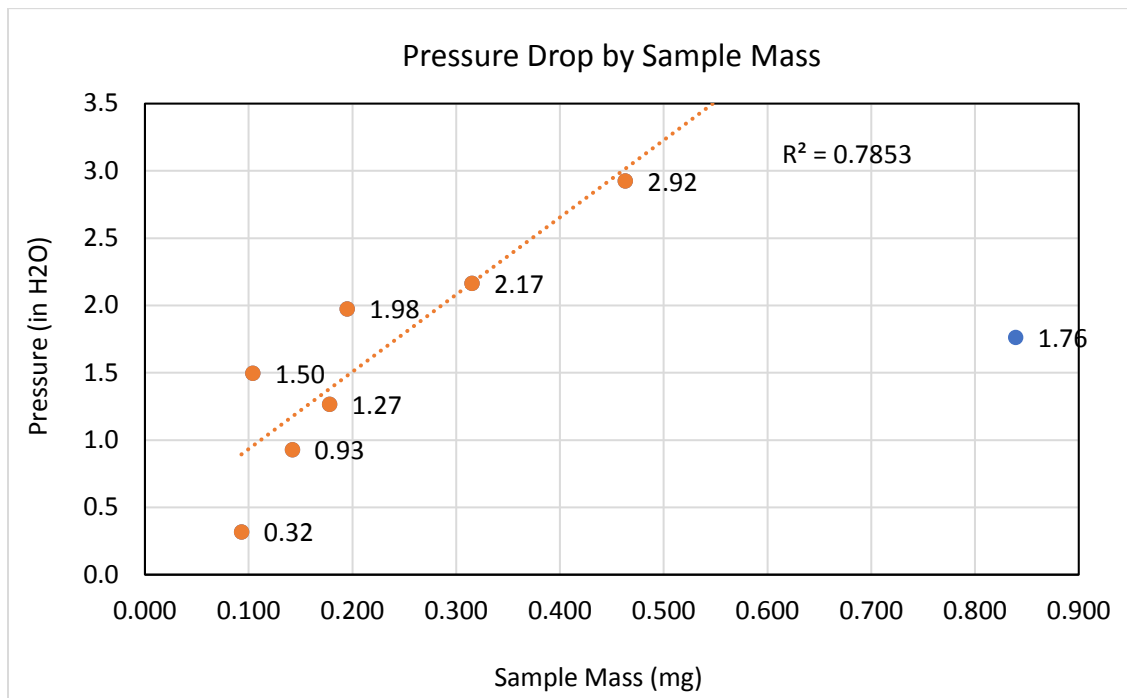

Figure 13. Relationship between particle collected mass and pressure build up on the filter in TDS.

We characterized the effect of flow rate on the pressure drop created by the polycarbonate membrane filters utilized by the TDS. Using Y shaped connectors, we measured the pressure drop for a set of three TDS cassettes whose values were averaged. Pressure data collection started at 0.1 L/min and ended at 4
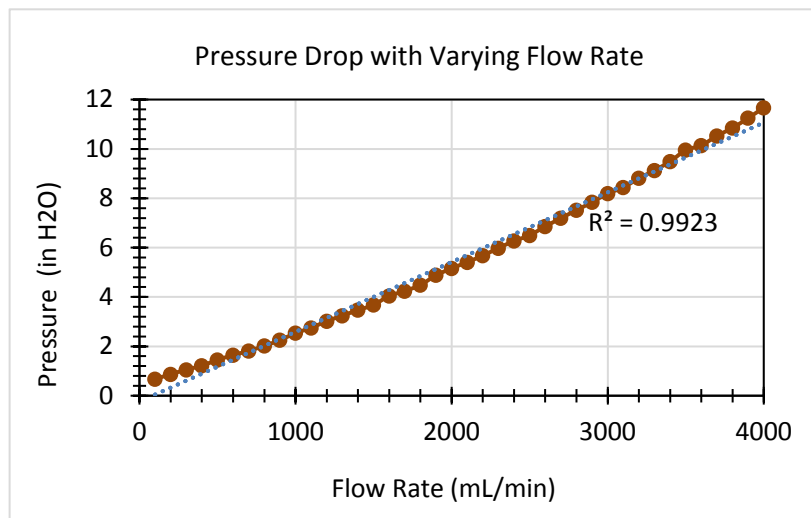
Figure 14. Pressure drop affected by flow rate in TDS.

L/min, with a measurement taken for every 0.1 L/min change in flow rate. As seen in Figure 14, the effect of flow rate on the pressure drop within the TDS provided evidence of a direct relationship. As the flow rate increased, a predictable increase in pressure drop was observed. The magnitude of the pressure changes due to flow rate observed in this study were greater than the observed changes in other experiments examining heavy particle loading. The pressure drop observed for the TDS was lower than that seen in other experiments when an open-faced cassette was used in place of the TDS.

We further evaluated long term sampling with a 16 hour particle loading test. We observed that the pressure drop gradually increased for all samplings as sampling time increased, as shown in Figure 15. The aerosol concentrations during this 16 hour sampling experiment are shown in Figure 16. The open faced 0.3 L/min sampling cassette was observed to have the lowest overall change in pressure throughout the experiment, at 0.58 in H_2O. The next lowest change was the TDS with 2.38 in H_2O. The open-faced 2 L/min sampling cassette was observed to have the highest pressure change of 3.80 in H_2O. This trend in pressure drop by sampler type was mirrored by the masses collected by each sample, as seen in Table 6. The differences in the pressure changes may be explained by the size selective inlet of TDS and the flow rate. The open-faced cassette effectively has no selection, thus allowing large particles and agglomerates to be collected, and, as expected, it showed the lowest pressure drop. These large agglomerates may create a lattice causing further particles to collect while still allowing air to flow through the filter. The TDS has an approximate cut point diameter of 4 µm with a theoretical maximum of 8 µm particles entering the cassette. The small air inlet and closed face cassette resulted in a greater increase in the pressure drop throughout the experiment.
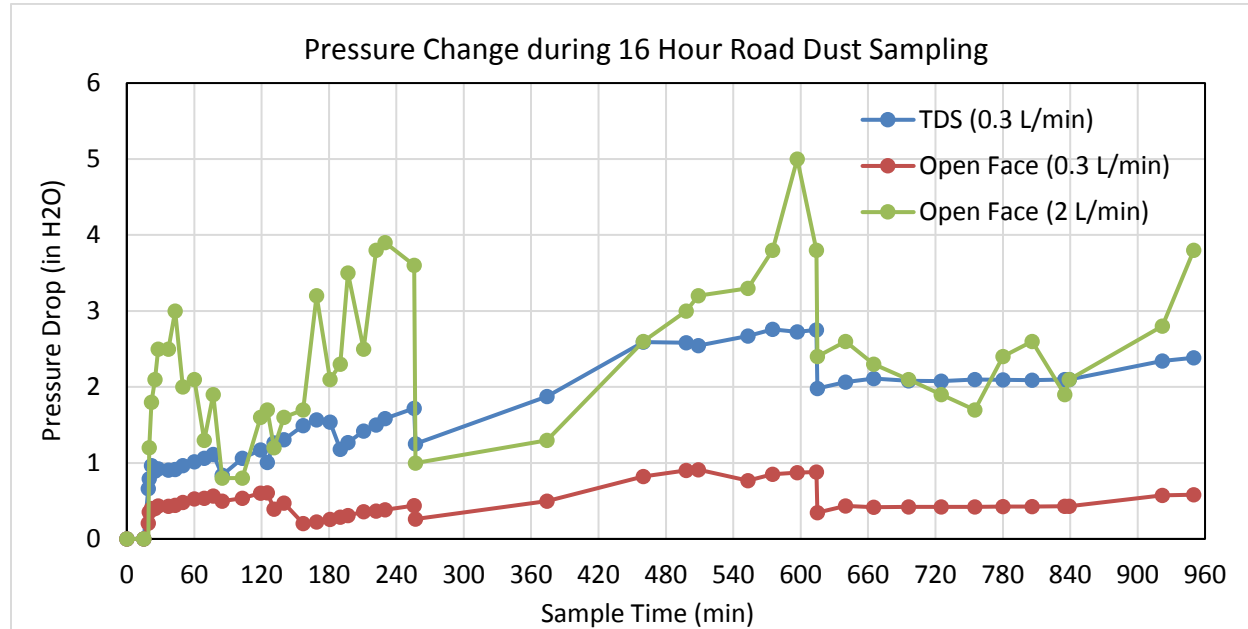

Figure 15. Pressure changes during 16 hour sampling with road dust, using a TDS.

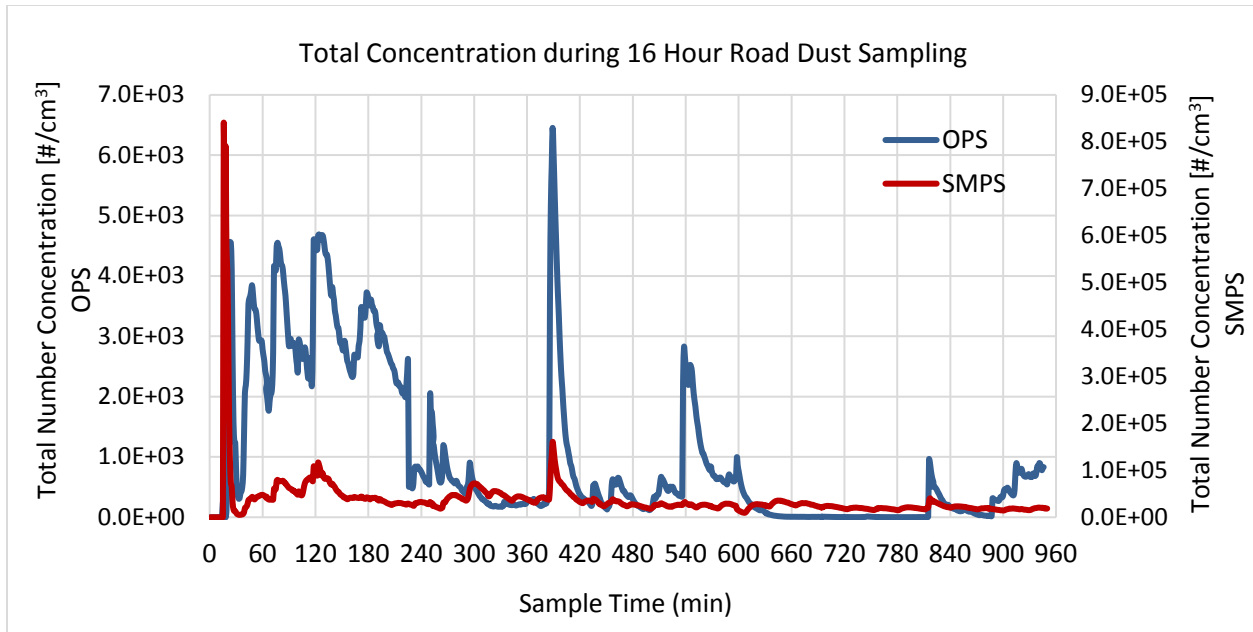Note: Pressure change was adjusted according to baseline pressure, owing to the known operating flow rate.

Figure 16. Total particle number concentration during 16 hours of road dust sampling.

Table 6. Variables and corresponding results of sampling loading tests

Sampler	Collected Mass (mg)	Flow Rate (L/min)	Pressure Change (in H_2O)	Sample Time (min)
TDS	0.67	0.3	2.38	960
25 mm Open Face	0.50	0.3	0.58	960
25 mm Open Face	6.70	2.0	3.80	960
Instrument	Average Concentration ± 1 Standard Deviation			
SMPS	36900 ± 494			
OPS	996 ± 1301			

5.3 Results of sensor performance

5.3.1 Sensor response with road dust

Numerous experiments (> 30) were performed to test several generations of sensors and the device. Figure 17 shows the time-response of a sensor device during two tests: one using road-dust and the other with the same airflow but without particles. At the beginning of each test, 5 min of background running (without airflow) and 15 min of airflow without particles were performed. After the tests ended, an additional 10 min of background running was performed. A clear differential response was observed, indicating that the sensor capacitance was stable enough for particle detection. Figure 17b shows an increase in sensor capacitance after testing, in agreement with positive shifts in counting from the readout circuit. The tested sensor was inspected with a scanning-electron microscope. Figure 18a shows images of a capacitance sensor exposed to a comparable flux of particles. Whereas most particles had sub-micrometer diameters, a few larger particles were observed. Figure 18b indicates that those larger particles were the agglomerates of sub-micrometer particles rather than single particles. The number of particles observed from the SEM image was calibrated according to the capacitance shift from Figures 17b and 18a, using Equation 1 below.

$$\frac{\Delta C \ (@ \ 1kHz)}{\# \ of \ particles \ on \ sensor} = \frac{0.137 \ pF}{12,993} \approx 10 \ atto \ Farad (10^{-18})/particle. \tag{1}$$

Ciccarella et al. (Ciccarella, Carminati et al. 2016) have demonstrated a particulate matter sensor using CMOS technology and have shown that a 5-μm diameter mineral talc particle can shift the capacitance by 10 aF. This finding is in good agreement with our calculation of capacitance shift. In addition, it demonstrates that comparable performance can be achieved by using low-cost fabrication methods rather than the high-cost CMOS process.

(a) (b)
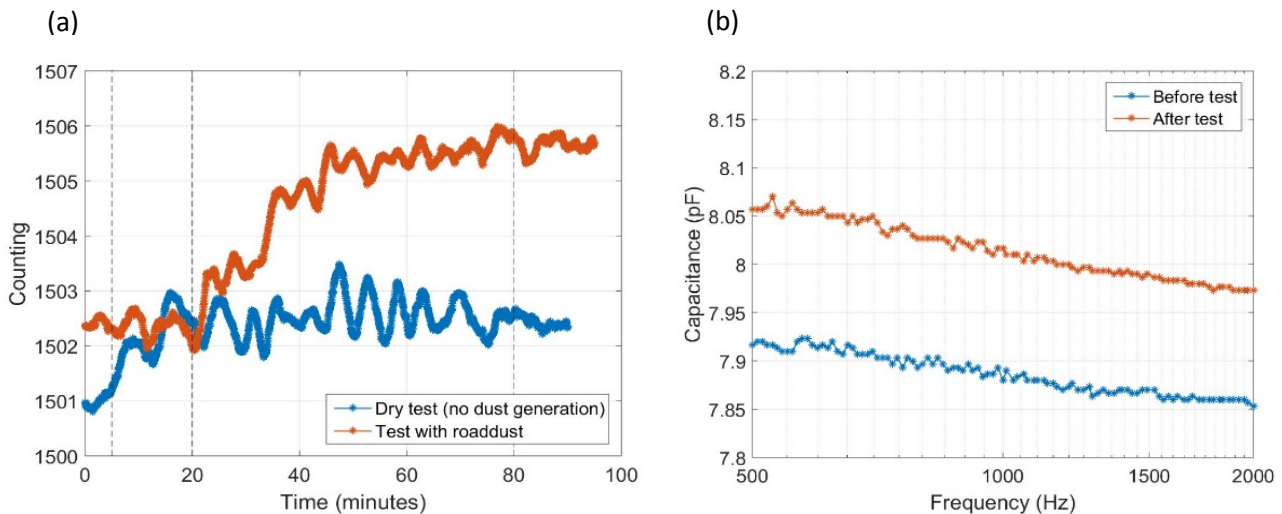
Figure 17. a) time-response of an integrated sampler, comparing 1) test with road dust and 2) a "dry" test, without particle generation. A clear differential response was observed for the case in which particles were generated in the chamber volume. b) Capacitance shift before/after testing, as measured by a laboratory capacitance meter. The positive shift in capacitance is consistent with increased counting.
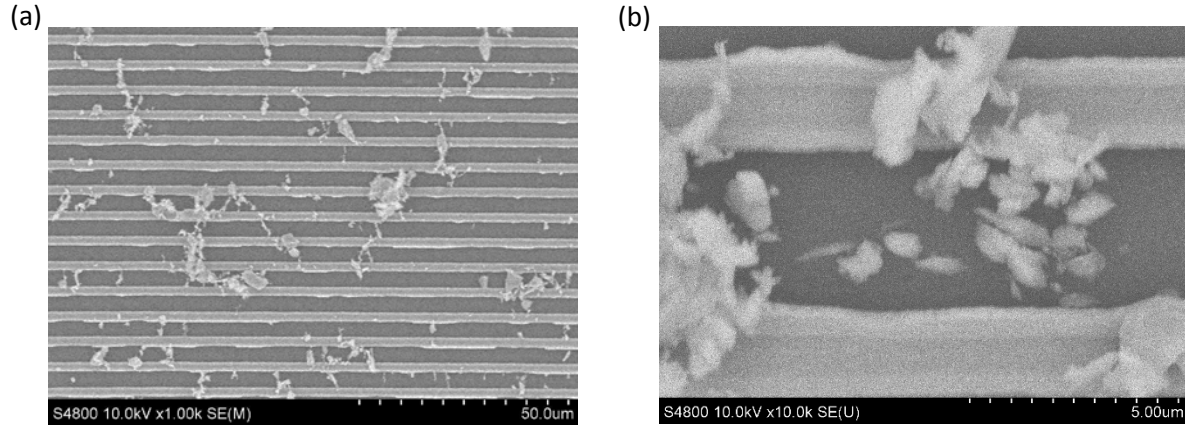
Figure 18. a) SEM image of particles deposited on a capacitance sensor after exposure to comparable particle flux. For reference, the lines and spaces in the image are approximately 3 microns. b) a magnified SEM image showing agglomerates of sub-micron particles.

5.3.2 Particle concentration and sensor response evaluation

To evaluate the sensor response with respect to collected particle concentration, we measured the filter weight before and after testing, by using a gravimetric method. The average concentration during testing was:

$$\frac{Collected\ particle\ mass}{Sampling\ volume} = \frac{0.08\ mg}{0.3 L/min * 60\ min} = 4.43\ mg/m^3\ . \tag{2}$$

Because the simulation study showed a radial dependence of particle distribution on the filter, it was necessary to calculate the volume fraction of particles on the sensor for precise evaluation. For ease of calculation, three representative particles (diameters of 1 μm, 5.8 μm and 9.0 μm) were chosen, and it was assumed that same amount of silica particles was collected. The volume fraction by radius was calculated from the simulation results of the cumulative population, as shown in Figure 19. That is:

i) r ≤ 1 mm
$$0.05 \times 1\ \mu m^3 + 0.15 \times 195\ \mu m^3 + 0.55 \times 729\ \mu m^3 = 430.25\ \mu m^3 \tag{3}$$
ii) r ≤ 4 mm
$$0.3 \times 1\ \mu m^3 + 0.7 \times 195\ \mu m^3 + 0.95 \times 729\ \mu m^3 = 829.35\ \mu m^3 \tag{4}$$
iii) r ≤ 5.5 mm
$$0.4 \times 1\ \mu m^3 + 0.85 \times 195\ \mu m^3 + 0.98 \times 729\ \mu m^3 = 880.57\ \mu m^3 \tag{5}$$
iv) r ≤ 10 mm
$$1\ \mu m^3 + 195\ \mu m^3 + 729\ \mu m^3 = 925\ \mu m^3 \tag{6}$$

Figure 20a shows the calculated volume fraction by radius. The results indicate that 47% of the entire volume was collected on the filter within r ≤ 1 mm, and 90% of the volume was collected within r ≤ 4 mm. Figure 20b shows a clear image wherein a high portion of particles was collected at the center area, and the concentration decreased with distance from the center. In addition, these results show that the sensor and

interface board do not interfere with particle collection, except that the relatively clean area at the lower side of the filter indicates the sensor and interface board location. Because the sensor is located in the range of 4 mm $\leq$ r $\leq$ 5.5 mm, the volume fraction of sensor area is:

v) 4 mm $\leq$ r $\leq$ 5.5 mm

$$(0.95 - 0.90) \times \frac{1.6\ mm^2\ (yellow)}{\pi \times 5.5 mm^2 - \pi \times 4 mm^2\ (red)} = 0.05 \times 0.04 = 0.002 \approx 0.2\% \tag{7}$$

Among the collected particles, only 0.2% of the entire volume was responsible for sensor response. Therefore, our sensor proved detection capability with a small portion of particles as well as selectivity for small particles. This result also emphasizes the importance of sensor location and the size of the sensor. Further improvements will be feasible by modifying the size and location in the next generation sensors.
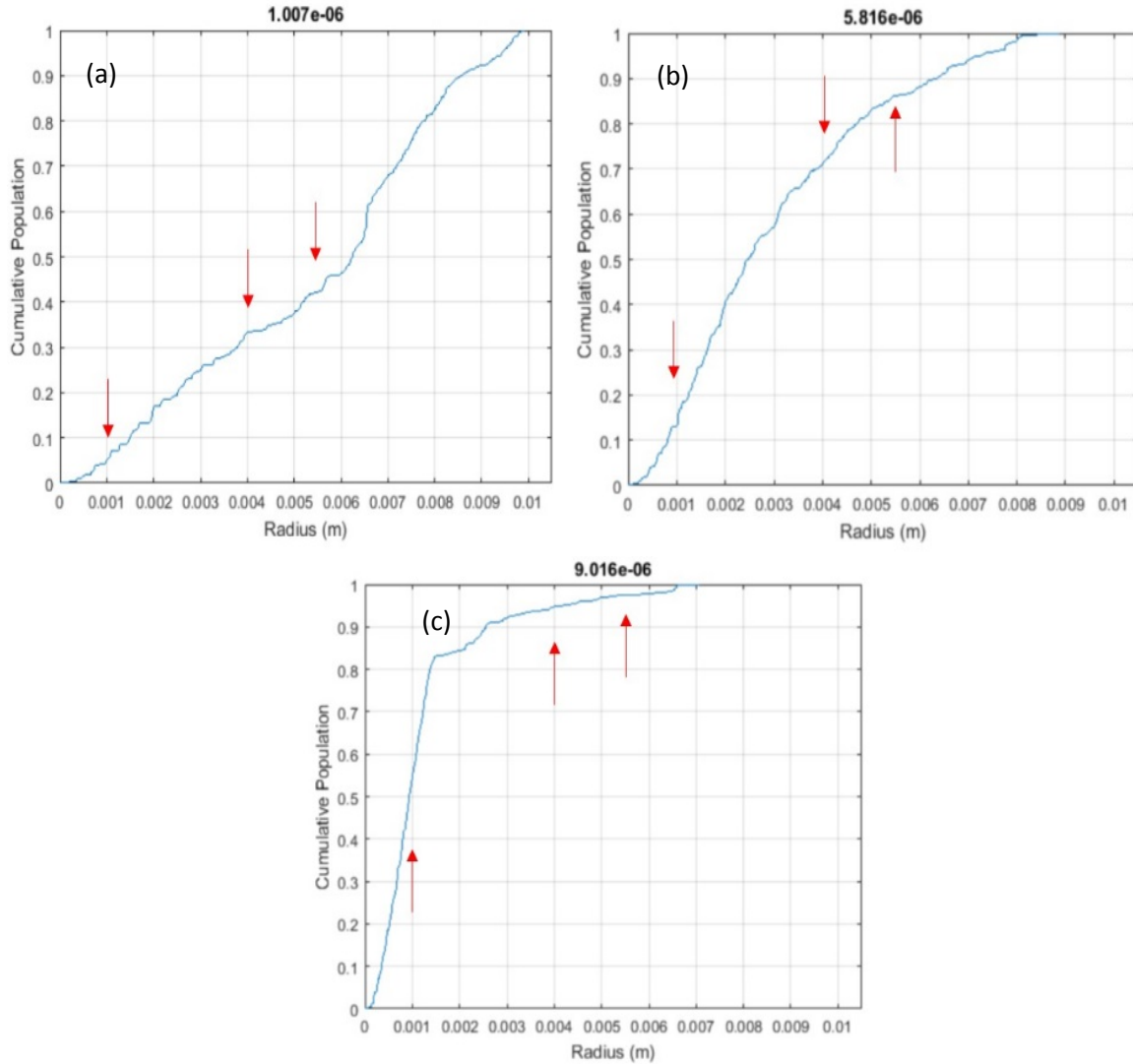
Figure 19. Cumulative population by radius. a) 1 μm-diameter, b) 5.8 μm-diameter and c) 9.0 μm-diameter. Arrows (red) indicates cumulative population at r = 1 mm, r = 5.5 mm and r = 9.0 mm.
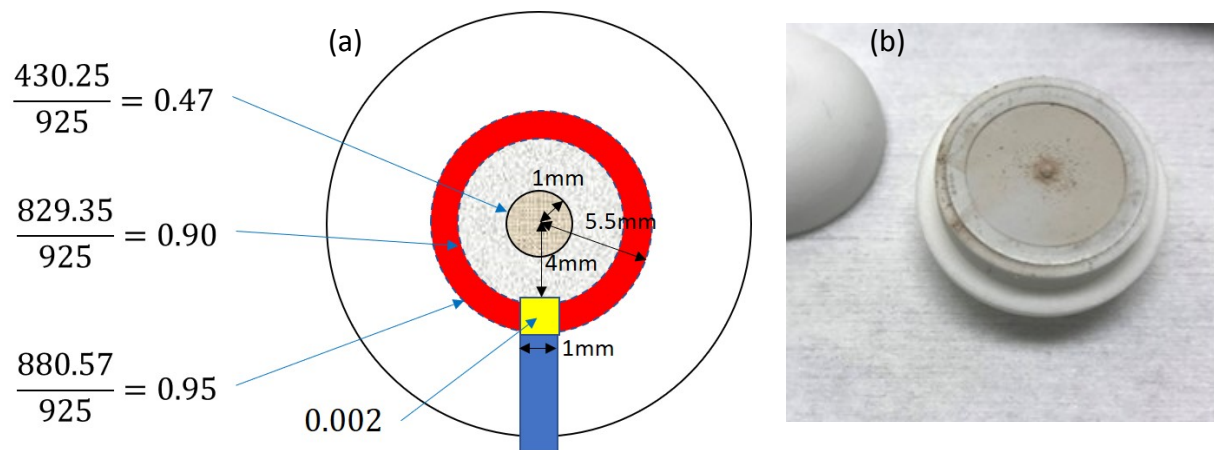
Figure 20. a) Volume fraction by radius. About 47% of the volume concentrated within r ≤ 1 mm, 90% of the volume concentrated within r ≤ 4 mm, and 95% of the volume concentrated within r ≤ 5.5 mm. The volume fraction on the sensor was 0.2% of the total volume. b) Photograph of the filter after testing. A high proportion of particles was collected at the center area, and the concentration decreased with increasing radius.

The assembled sampling device was also tested at the CSU laboratory, and example images with road dust particles deposited on the sensor after a 3 hour sampling is shown in Figure 21. The sampled filter was estimated to collect 0.45 g of road dust after a 3 hour sampling, which is equivalent to 8.3 mg/m^3 mass concentration. Our sampled filters were estimated with mass concentrations ranging from approximately 5 to 9.7 mg/m^3 after 3–4 hours of sampling with similar airborne road dust concentrations. This is approximately three to six times the current mine dust exposure limit (1.5 mg/m^3). The airborne road dust concentrations and size distribution during a 3 hour sampling are shown in Figure 22. The airborne dust concentrations in the submicrometer size range (10–420 nm by SMPS) were in millions of particles/cm^3;
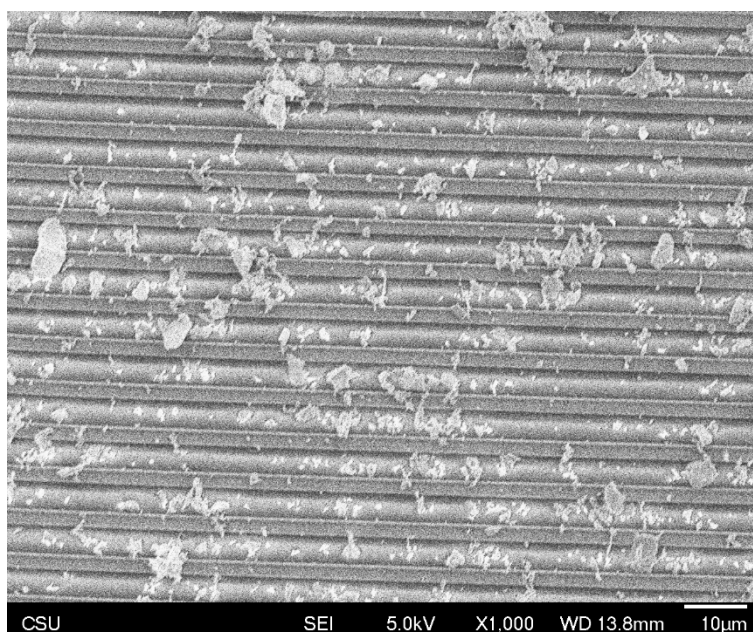
Figure 21. SEM image of the sensor with road dust deposited on the top and between the sensor strips.

and the concentrations in the larger sizes (0.3–10 μm by OPS) were in thousands of particles/cm^3. These ranges of particle concentrations represent the dust level ranges in the mining environment.

The particle total number concentrations over time as seen in Fig. 22a showed that OPS measured a high concentration with the peak appearing at the beginning (within 20 min) of aerosol generation, and the SMPS showed the highest concentration about 30-40 min after the aerosol generation. It was typical to see at the beginning that micrometer sized road dust particles were generated and released more than smaller ones from this generator, soon followed by a lot more small/sub micrometer sized particles. After the small particles (< 420 nm) were released and measured, approximately at the 50 minute as marked with an arrow in Fig. 22a, those small particles began to agglomerate and form larger particle agglomerates in the air in such a high concentration environment because of coagulation of particles. Aerosol particles collide due to their random motions and coalesce to form larger chains of flocs made up of many particles. The Brownian motion of particles, turbulence, presence of a shear field, and external forces such as gravity and electrical forces could cause coagulation. Smaller particles have stronger Brownian motion. The aerosol will approach equilibrium with the increased number of larger agglomerates and reduced number of small particles as seen at approximately 80-90 minutes. As noted in Section 5.1.6., the dust feeder was run for 30 second intervals every 30 min during particle generation. The equilibrium was seen at the time close to the end of the 30 min cycle, then another spike of aerosol concentration with a large amount of small particles was generated. The proportion of different particle sizes changed and the cycle was reset. This aerosol behavior is the reason for increased concentrations by OPS measurement and then remaining at the high level, however, the small particles measured by SMPS showed the spike of increase at the time of generation and were reduced over time afterward. However, the concentration was still high at 10^5 particles/cm^3 or greater. A similar aerosol behavior was seen in Fig. 25a, and aerosol shown in Fig. 25a was generated every 15 minutes.
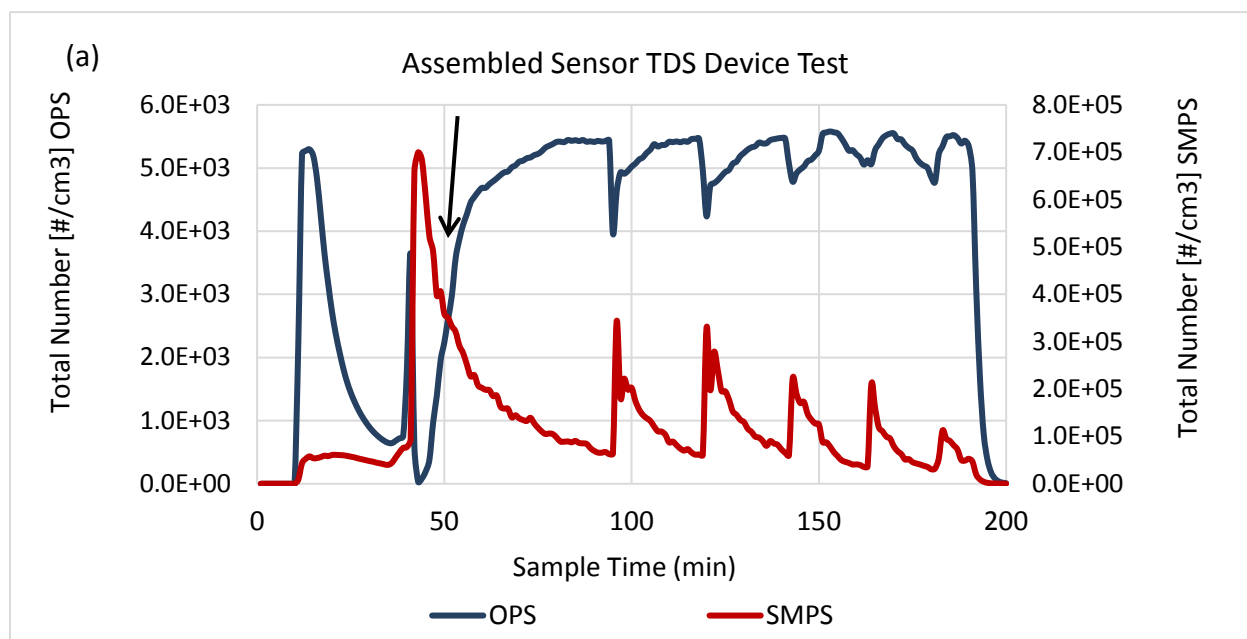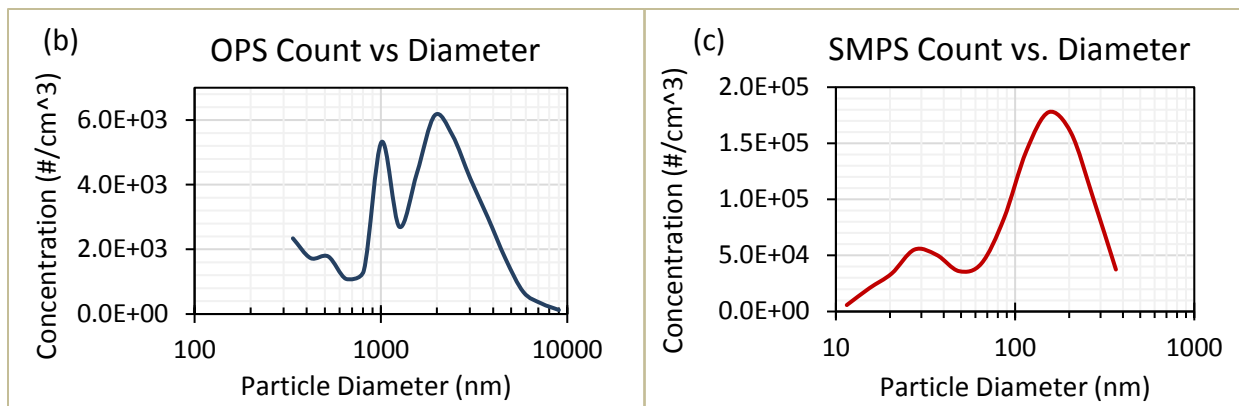
Figure 22. Airborne road dust measured with a real time particle counter during sampling, a) total particle number concentrations measured every minute with OPS and NanoScan SMPS, b) particle number concentration and size distribution in the range of 0.3 to 10 μm, c) particle number concentration and size distribution in the range of 10 to 420 nm.

The proof-of-concept device was enclosed in a clear acrylic box, and all components were secured. This assembled device was tested at the Colorado State University (CSU) laboratory to establish the correlation between the sensor signals and the particle concentrations. As seen in Figure 23, the device (marked in the yellow rectangle area) was covered with a plastic bag to avoid surface contamination. It was located side by side with the tubing inlets of real time particle counters for three hours of dust collection.
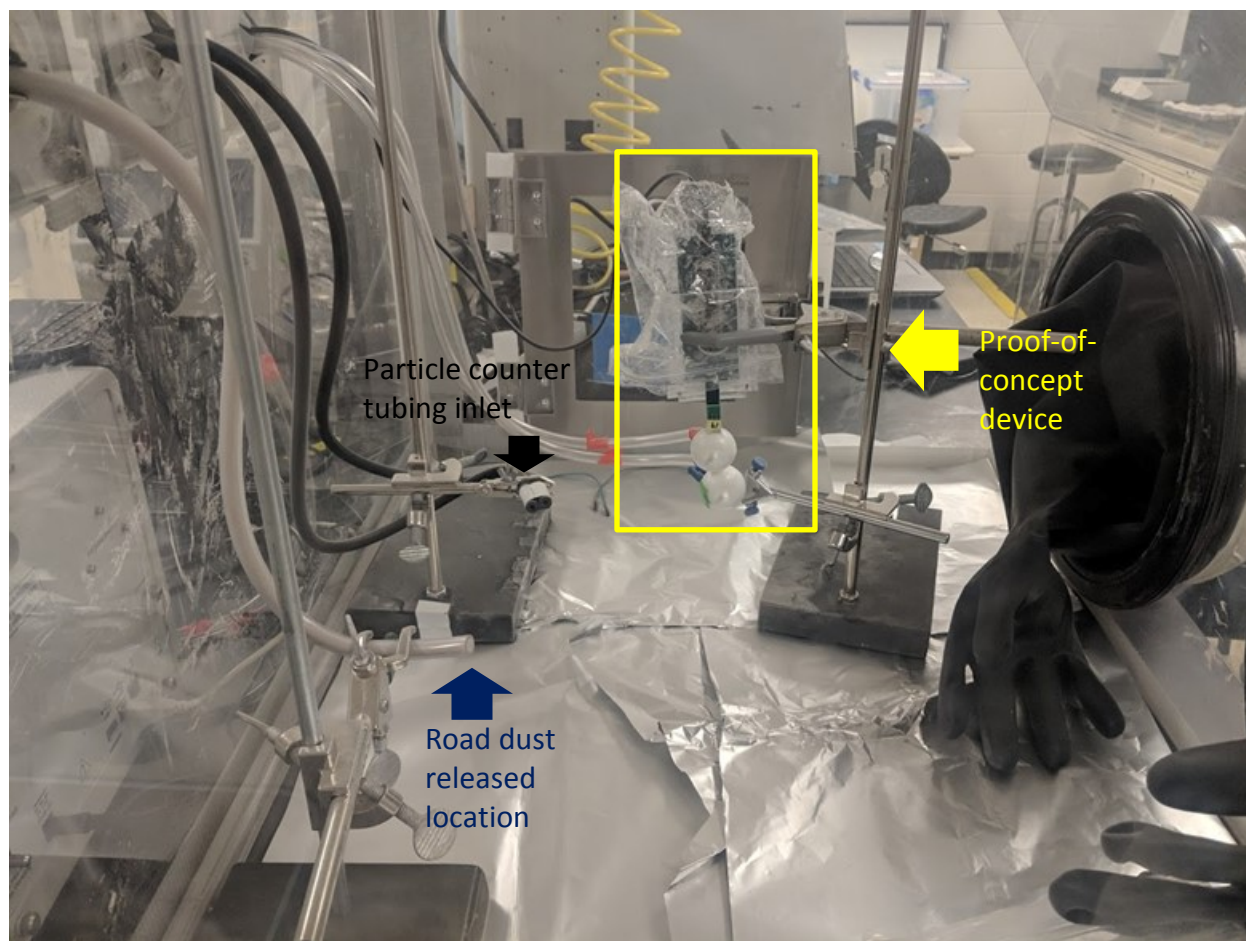
Figure 23. Experiment setting for assembled proof-of-concept device. Road dust (silica dust) airborne particles were generated and released through the tubing into the glovebox.

As shown in Fig. 24a, the sensors had very similar sensor responses compared to the results in Fig. 17a in which positive counting shifts were observed with tests at Purdue laboratory. A more linear response in Fig. 24a was observed during three hours of testing at CSU because of the uniform particle generation system employed. The particle cumulative total number concentrations during this test are presented in Fig. 24b. The concentrations in the sub micrometer range of 10-420 nm were measured by a NanoScan SMPS. These began at a concentration of 10^4 to 10^5 and increased to a concentration exceeding 10^7 particles/cm^3. The number of concentrations in the sub micrometer to micrometer range (0.3-10 μm) measured by OPS began with a concentration of approximately 10^3 particles/cm^3 and increased to nearly 10^6 particles/cm^3. The total concentrations measured every minute by each instrument are shown in Figure 25a, and the size distribution and concentration of each size channel are presented in Figure 25b and 25c. In this experiment, the aerosol was generated with 15 minute interval. As seen in Fig. 24b, the cumulative total concentrations gradually increased during the sampling period, and the sensor responded accordingly with increasing signals (Fig. 24a), indicating a strong correlation between particle deposition on the sensor and the sensor's responses. The total mass concentration after three hours of sampling was 9.7 mg/m^3, which covers the range of a miner's exposure during a work shift. Our results have demonstrated the success of this proof-of-concept device.

(a)　　　　Capacitance Sensor Signals Responding to Particle Collections
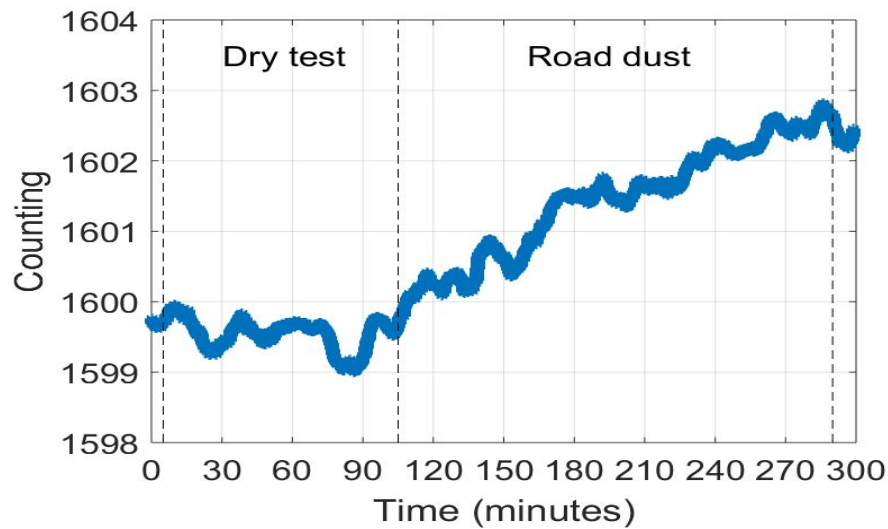
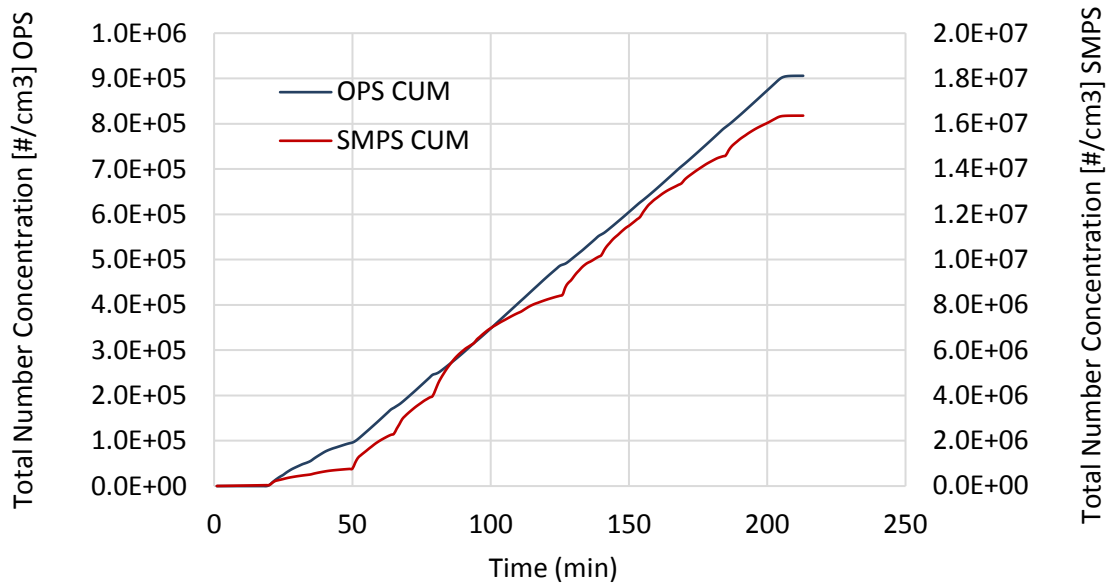(b)　　　　Cumulative Particle Number Concentration

Figure 24. Sensor responses and particle cumulative number concentration during the three-hour sampling test. (a) Capacitance sensor signals responded to the airborne road dust deposition in the sampling device; (b) Cumulative particle total number concentrations measured by OPS (left y-axis) and NanoScan SMPS (right y-axis).
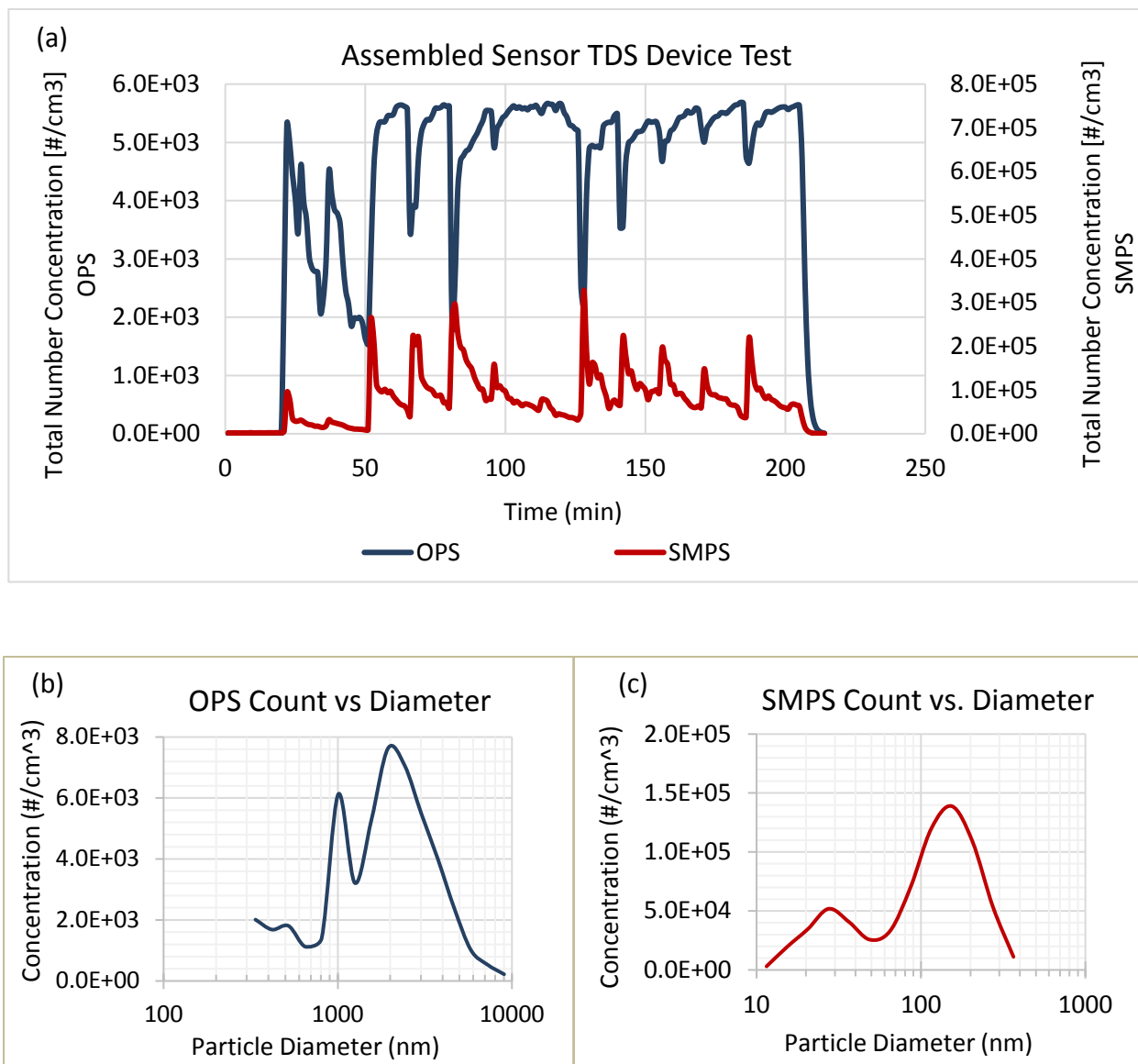
Figure 25. Airborne road dust measured using a real time particle counter during sampling for sensor response measurements, a) total particle number concentrations measured every minute by OPS and NanoScan SMPS, b) particle number concentration and size distribution in the range of 0.3 to 10 μm, c) particle number concentration and size distribution in the range of 10 to 420 nm.

5.3.3 Microheater characterization

The resistance heater integrated on the sensor/heater strip allows heating of the strip to a controlled elevated temperature. This is intended to mitigate effects of high and variable ambient humidity as well as to eliminate temperature-based drift in the sensor capacitance. As shown in Figure 26, we studied the stability of the sensor capacitance without (Figure 26a) and with (Figure 26b) the heater activated. The use of the heater resulted in a more stable sensor capacitance, thus enabling stable detection of a smaller quantity of deposited particles. We also studied the stability of the capacitance signal as a function of relative humidity at room temperature. As shown in Figure 27, the use of the on-board resistance heater significantly decreased the variation in capacitance over the range of 43–74% relative humidity (dew point of 5.6 °C to 18 °C), thus indicating that the capacitance sensor can operate over a range of ambient dew points.
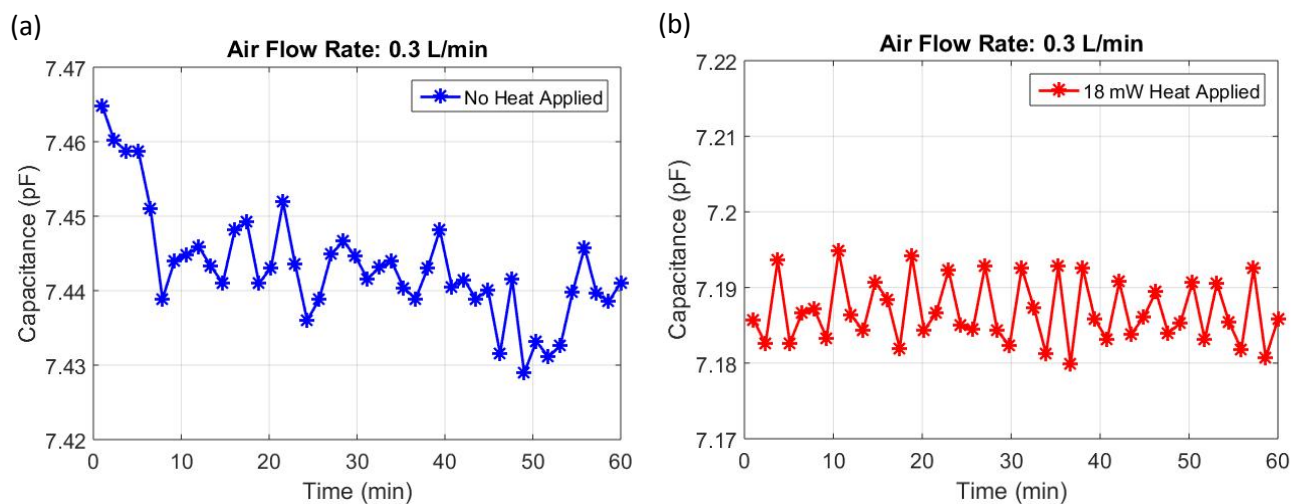
Figure 26. Capacitance sensor test a) without and b) with heating via a resistance heater. Tests were performed with a TDS, at constant flow rate.
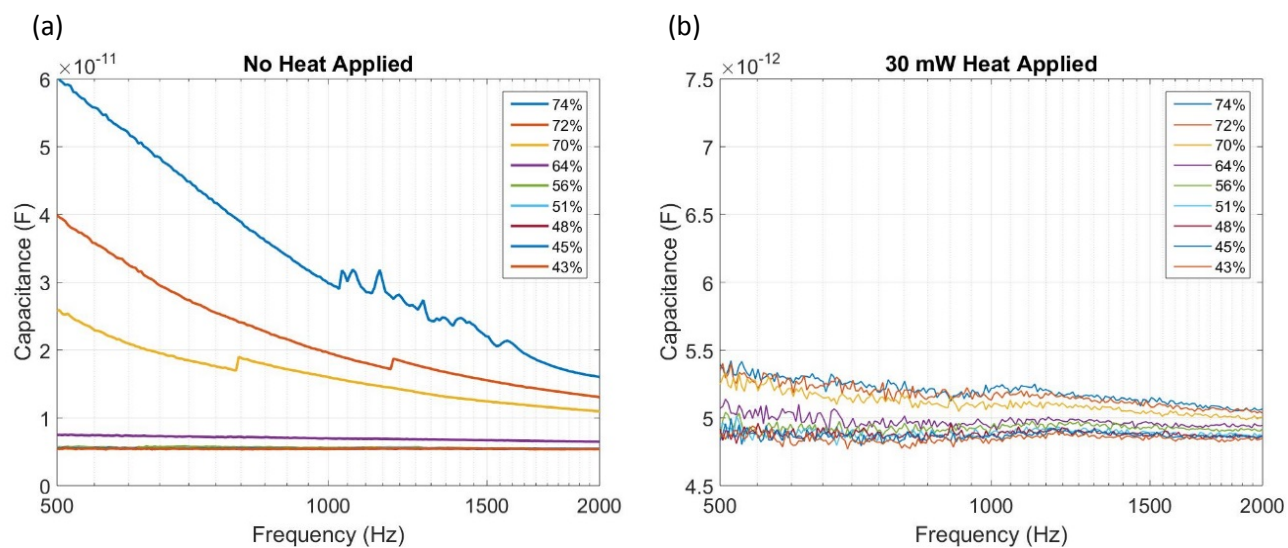
Figure 27. Capacitance response at different relative humidity levels a) without a heater and b) with 30 mW heater power. The stability of capacitance markedly improved specifically at higher relative humidity (or dew point).

5.4 Field sampling using a TDS for mine dust

We tested the TDS cassette (without a sensor) in the field, at the Edgar experimental mine, to sample mine dust from drilling activities and diesel engine exhaust from operating a locomotive. Some results of our tests were presented in the annual mining conference in Denver in 2019, and some results have been submitted to a peer-reviewed journal and are expected to be published in 2019. Mine particles were sampled and characterized by using the TDS, as shown in Figure 28.

According to our study, there is a major nanoparticle inhalation risk in the mining environment that is not well characterized by the currently employed methods of investigation. The highest concentration measured for drilling activity in the 10–420 nm range was 4.4×10^6 particles/cm^3 and 3.5×10^3 particles/cm^3 in the 0.3–10 µm range. These particles were identified to be composed of silicon, carbon and trace minerals. Nanoparticles from drilling were not present in the background concentrations within the mine. Regardless of the high concentrations, these particles are effectively massless when examined by gravimetric methods for evaluation levels of RPM. The effects of exposure to a nanoparticle rich atmosphere, as identified at the underground mine, must be further understood.

Figure 28. Image analysis of the TDS sample from the first ten minutes of drilling, a) overview image at 50× of the center of a TEM grid showing heavy particles, b) image of one grid space viewed at 400×, where a bimodal particle distribution can be seen, c) TEM image take at 6000× showing very fine particulates less than 100 nm in diameter, d) TEM image taken at 6000× of agglomerates, e) SEM image of a TDS filter showing the collection of very fine particulates, with a scale bar of 1 µm, f) SEM image showing very fine particles, with a scale bar of 100 nm, g) SEM image of a TDS filter showing large agglomerates, with a scale bar of 1 µm, h) close-up image of agglomerate microstructures, with a scale bar of 100 nm.
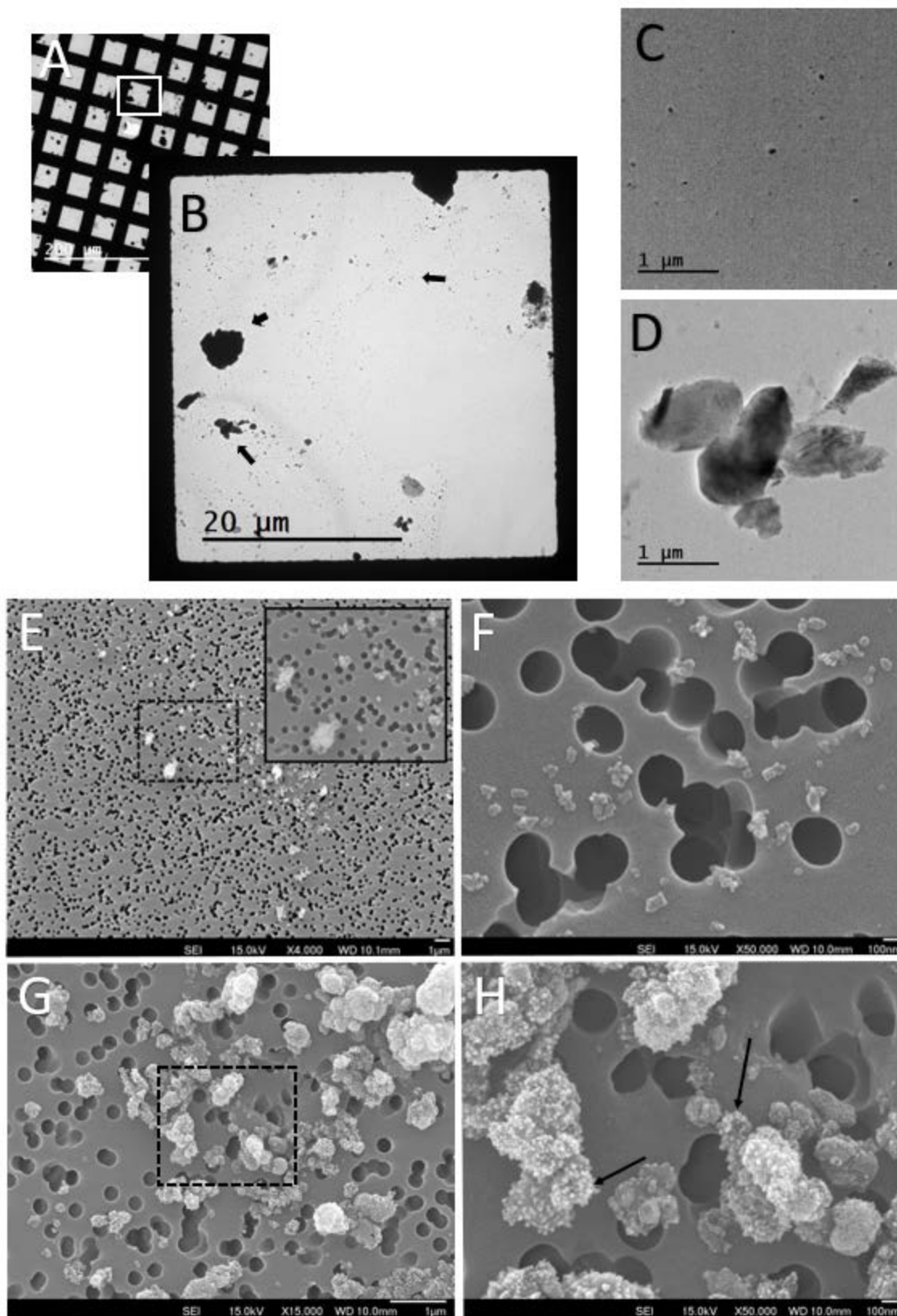
6.0 Technology Readiness Assessment

6.1 Sensor readout generation and future improvement

The current generation assembly is ~12 cm × 3.5 cm (including the sampler housing); it weighs approximately 37 g, and the readout board comprises a large portion. We estimate that this footprint can be downscaled by ~50% in future designs. The interface PCB facilitates the replacement of the sensor as well as the reuse of readout PCB. However, the sensor signal is highly influenced by the connection between the sensor and readout PCB. Use of a coaxial pin or latch-lock header would improve the interface electrically and physically. The current generation uses a micro-USB port for power and data transfer to a computer. In the next generation, wireless communication can be applied by using Wi-Fi or Bluetooth, and a commercial battery can be used for power.

6.2 Sensor generation development in the past, and strength and weakness of the current version

The first generation sensor was made by using a silicon wafer. Because silicon is the most commonly used material for microelectronic devices, reliable device production is an advantage. Moreover, it is a rigid substrate that enables easy and secure integration with PCBs and modified samplers. However, silicon substrates have a high parasitic capacitance, which affects sensor capacitance and substantially decreases sensor performance. We chose polyimide film for the current generation, because it minimizes the parasitic capacitance. The challenge of using polyimide film is to secure reliable production, because it is a flexible material. We optimized the fabrication process and are able to make 24 strips in a 3 cm × 4.5 cm area. This capacity can be improved by future process optimization.

Though we minimized the parasitic capacitance from the substrate, parasitic capacitance remained on the readout and interface PCBs. The fractional change in sensor capacitance is not purely reflected in the fractional change in the counting, owing to the parasitic capacitance. For instance, although the readout calibration using fixed capacitors estimated a resolution ~15 fF/count, the test results using road dust showed ~42 fF/count. Thus, further developments are necessary to maximize the fractional change in the sensor as well as to minimize the parasitic capacitance from the readout and interface boards.

6.3 Proposed necessary modifications and the pathway to achieve this goal

The current generation sensor was designed such that it minimizes the perturbation of air flow. Future modifications can be made by increasing the size of the sensor. This modification would not only increase the sensing area; increasing sensor capacitance can also help overcome parasitic capacitance from PCBs. Thus, the fractional change in capacitance will result in a larger fractional change in the counting. In addition, decreasing the electrode spacing or increasing the height of electrodes can increase the fractional change in sensor capacitance with respect to particles. Such a modification could be made by nanoscale patterning or electroplating of electrodes.
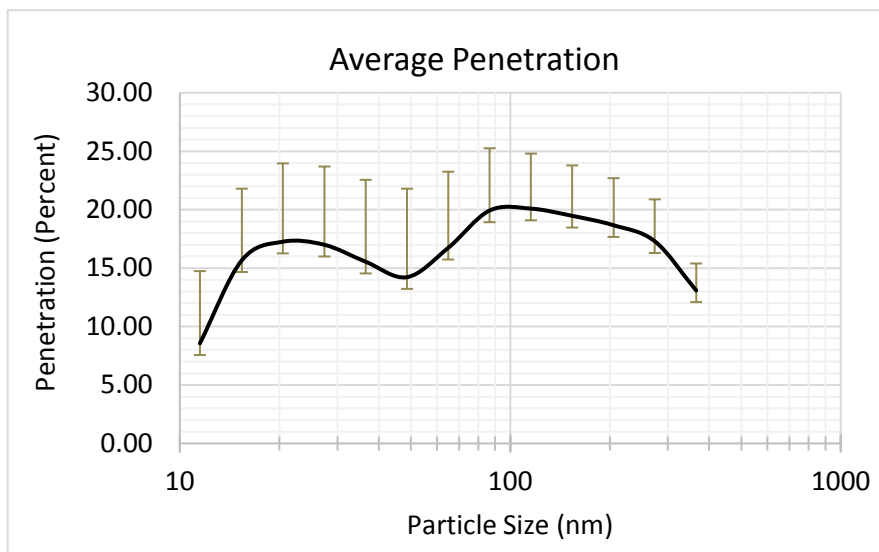
7.0 Appendices:

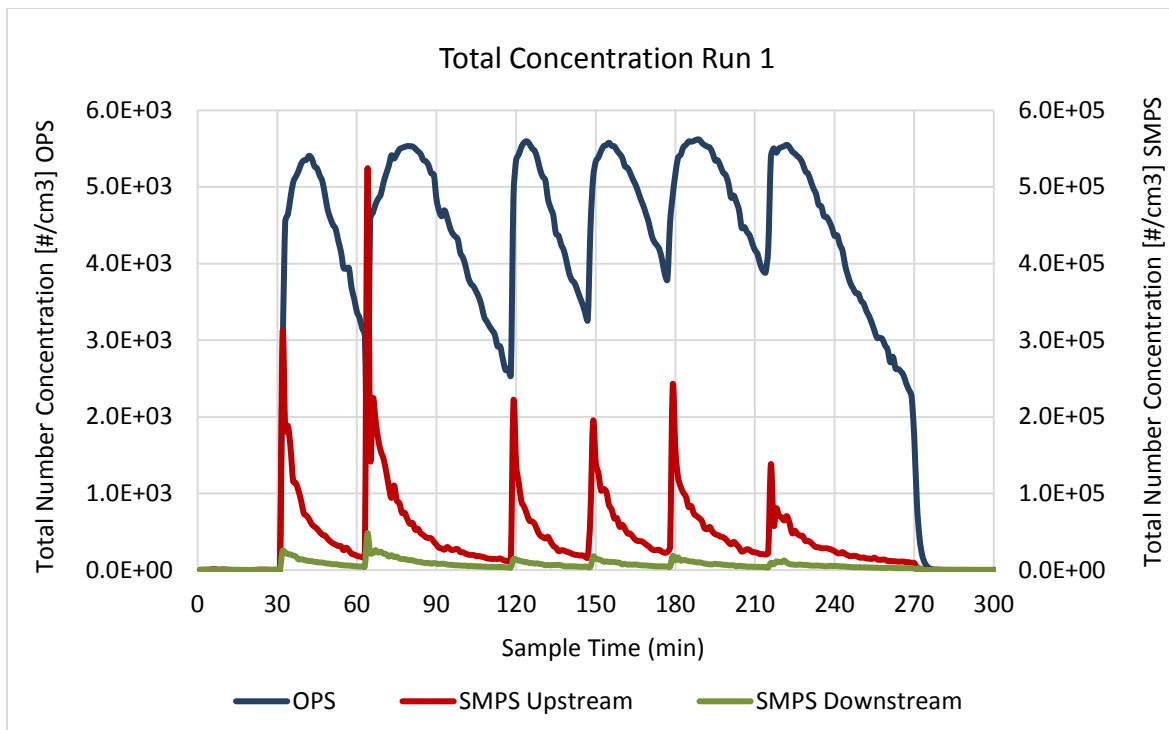Figure A1. Average particle penetration of three repetition for sizes less than 420 nm

Figure A2. Total particle number concentration of OPS and NanScan SMPS during entire first penetration experiment.
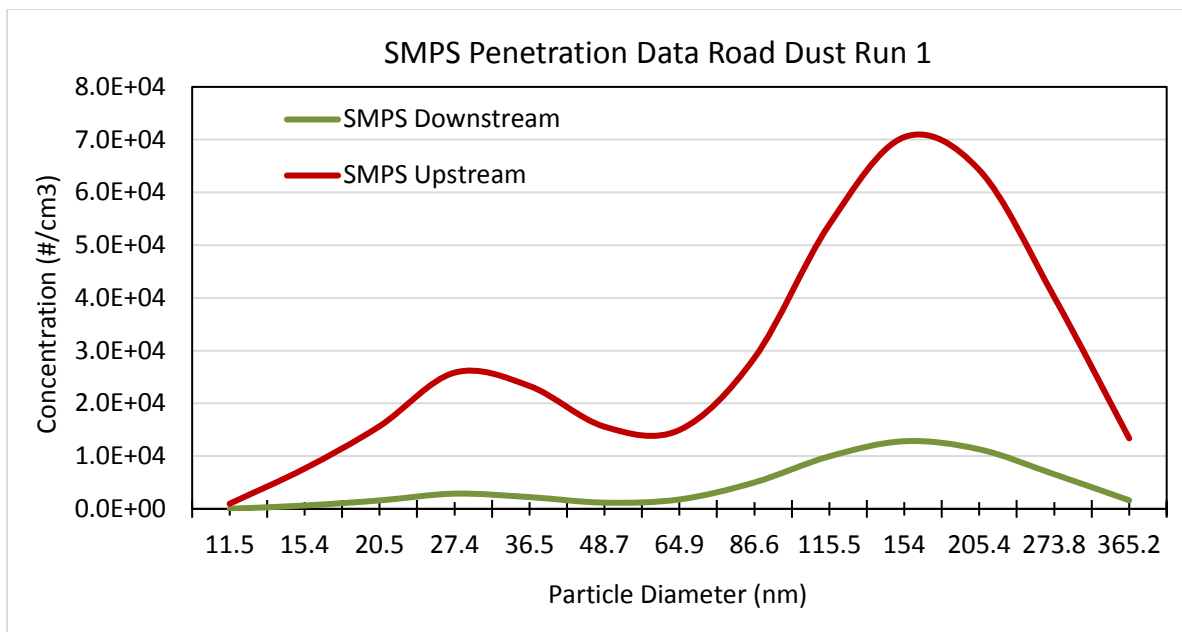
Figure A3. Particle number concentration and size distribution of OPS and NanScan SMPS during entire first penetration experiment.
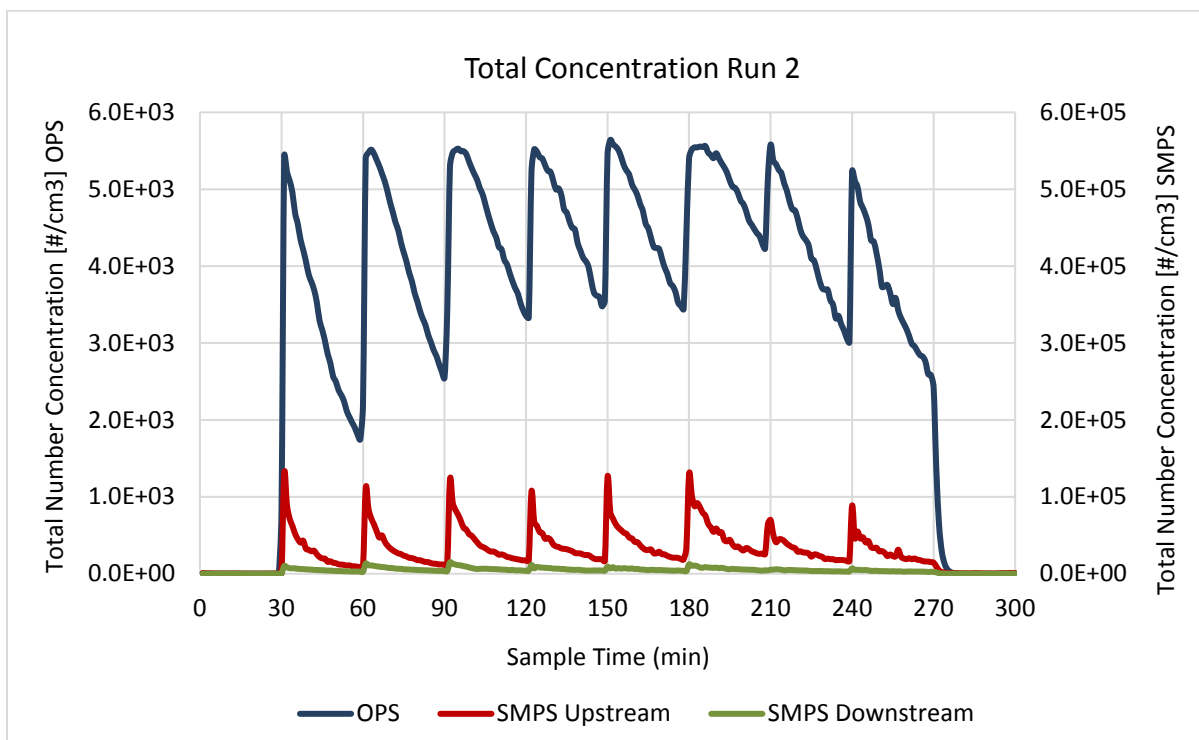

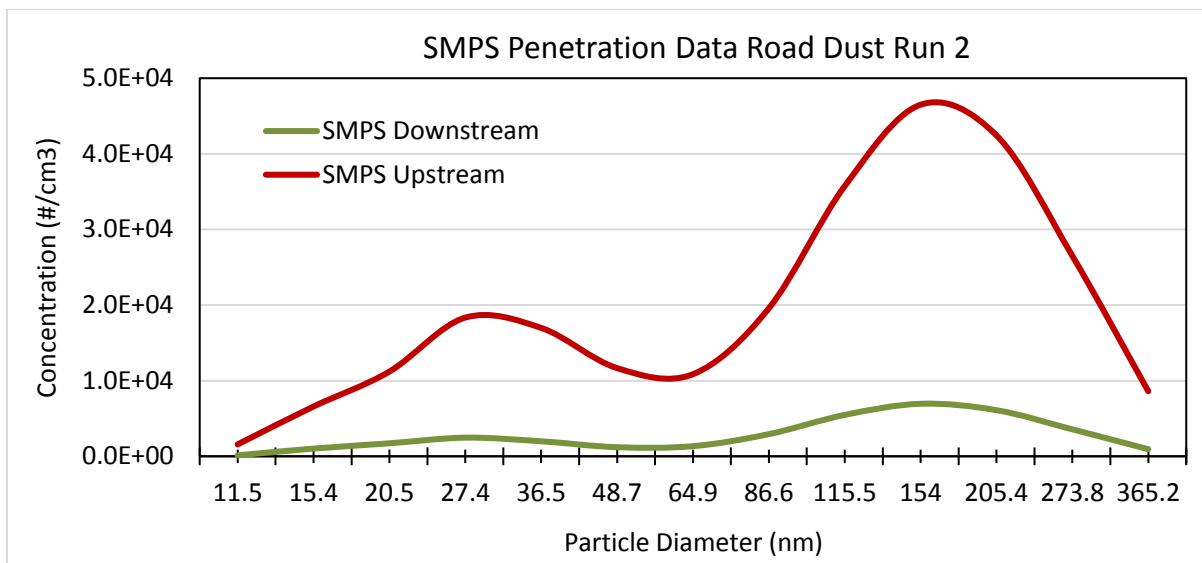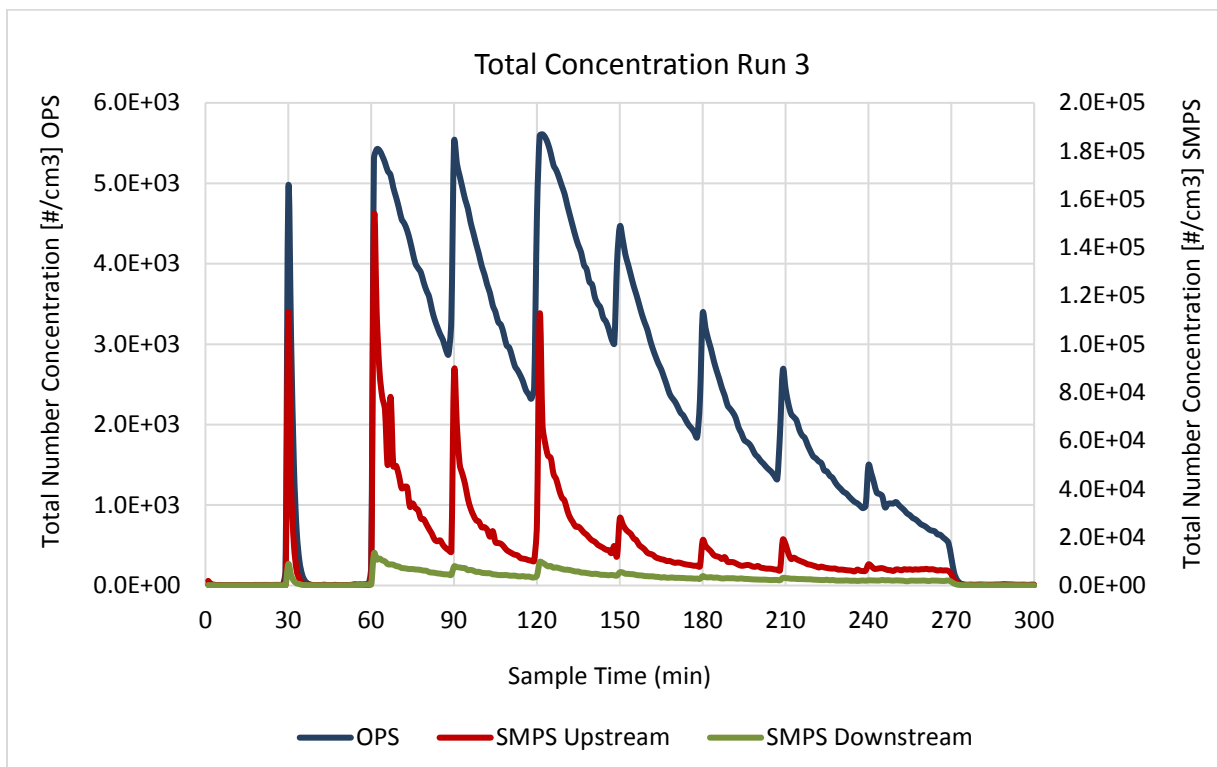Figure A2. Total particle number concentration of OPS and NanScan SMPS during entire second penetration experiment.
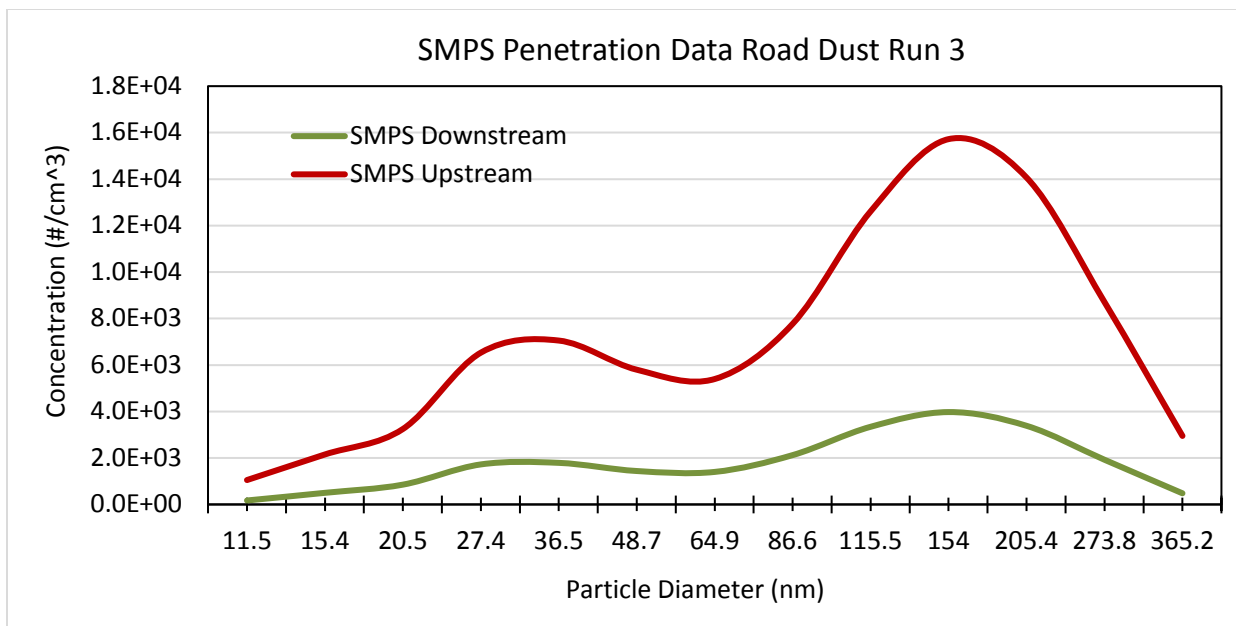
Figure A5. Particle number concentration and size distribution of OPS and NanScan SMPS during entire second penetration experiment.

Figure A2. Total particle number concentration of OPS and NanScan SMPS during entire third penetration experiment.

Figure A7. Particle number concentration and size distribution of OPS and NanScan SMPS during entire third penetration experiment.
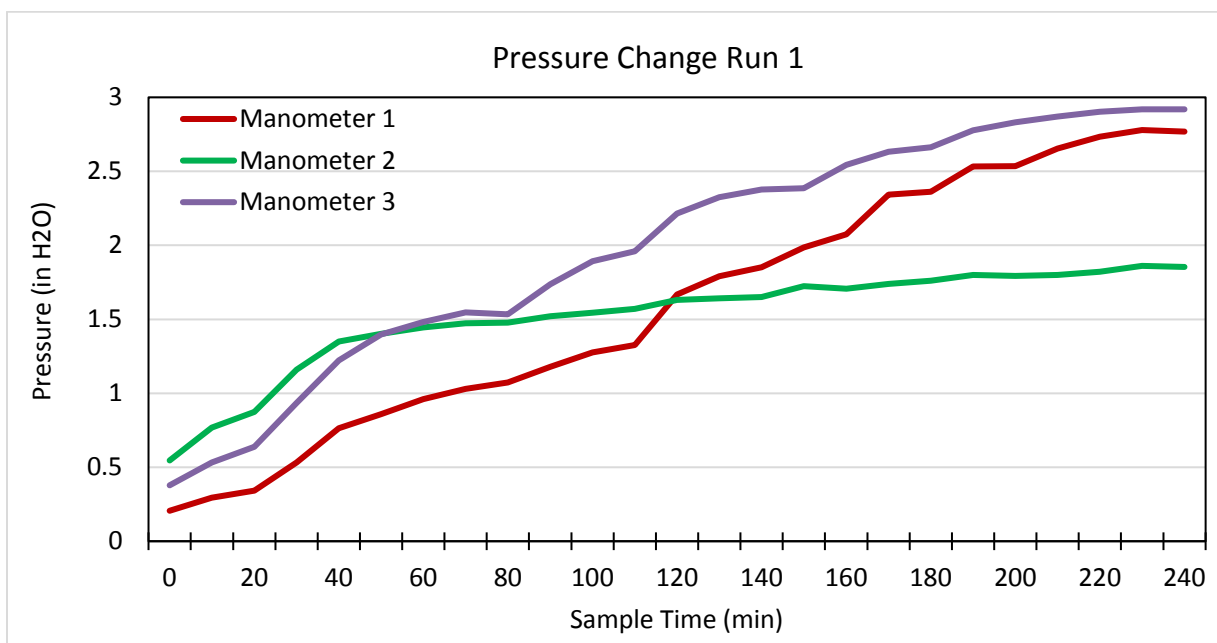

Figure A8. Pressure drop change during penetration experiment of entire first experiment.
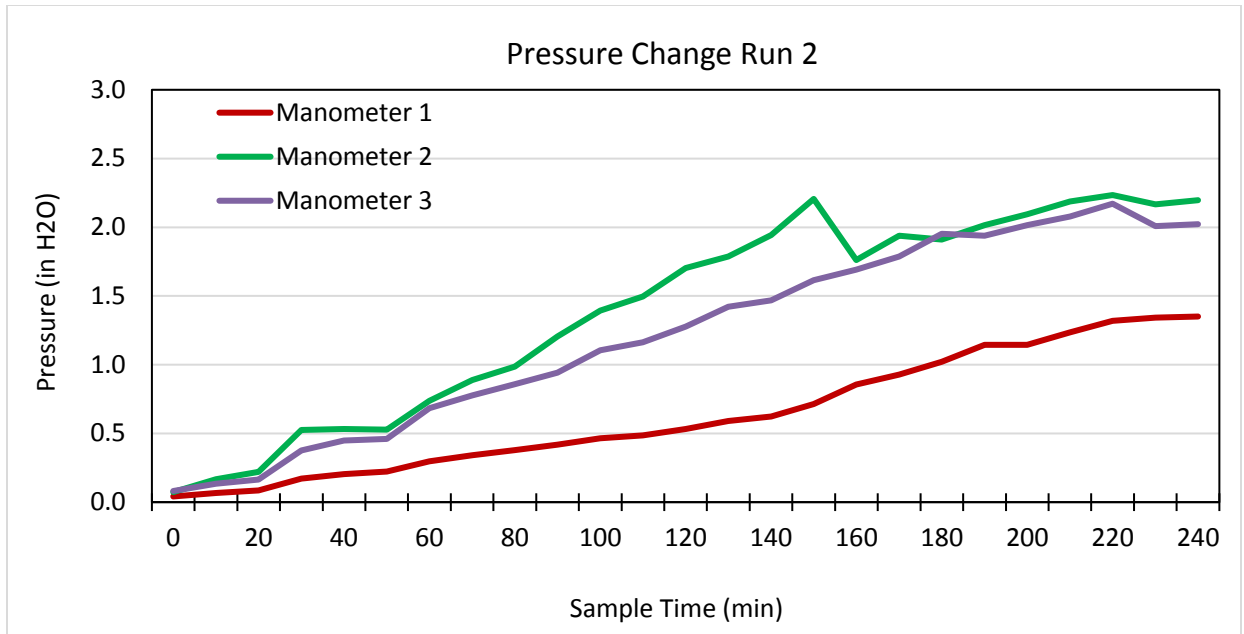
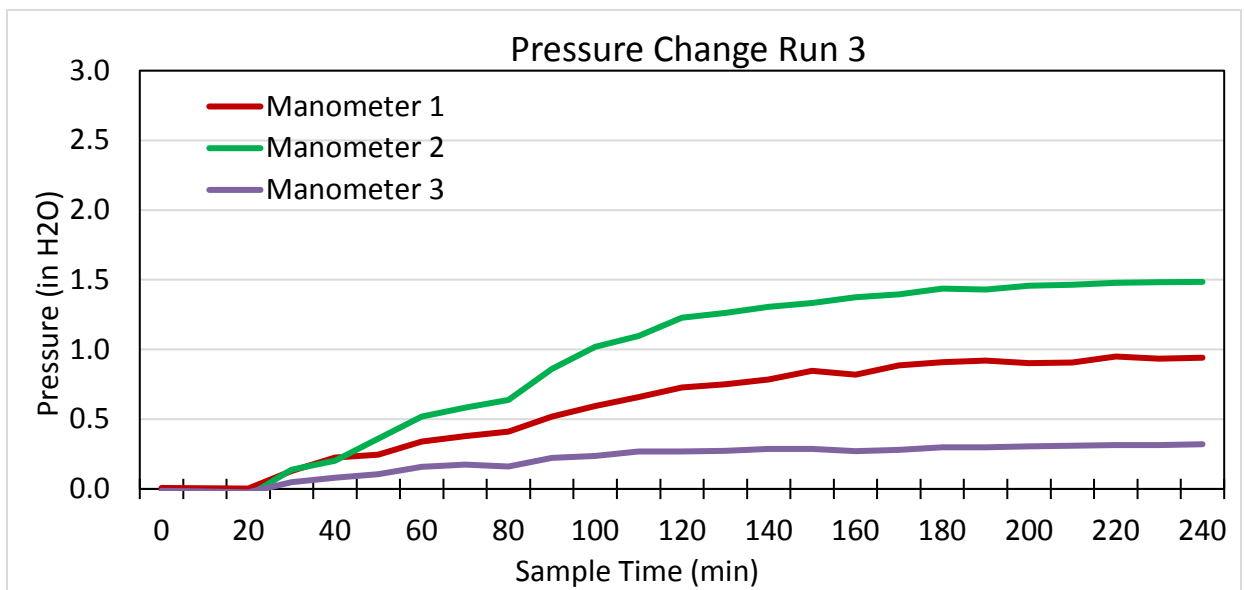Figure A9. Pressure drop change during penetration experiment of entire second experiment.

Figure A10. Pressure drop change during penetration experiment of entire third experiment.

8.0 Acknowledgement/Disclaimer

Reference

(2000). "New Directions: The suitability of tapered element oscillating microbalances (TEOMs) for PM10 monitoring in Europe. The use of PM10 data as measured by TEOM for compliance with the European Air Quality Standard." Atmospheric Environment **34**: 3209-3212.

Chan, S. H. and H. Y.S. (1999). "Measurements of particulate mass concentration using a tapered-element oscillating microbalance and a flame ionization detector." Meas. Sci. Technol. **10**: 323–332.

Charron, A., R. M. Harrison, S. Moorcroft and J. Booker (2004). "Quantitative interpretation of divergence between PM10 and PM2.5 mass measurement by TEOM and gravimetric (Partisol) instruments." Atmospheric Environment **38**: 415–423.

Ciccarella, P., M. Carminati, M. Sampietro and G. Ferrari (2016). "Multichannel 65 zF rms Resolution CMOS Monolithic Capacitive Sensor for Counting Single Micrometer-Sized Airborne Particles on Chip." IEEE Journal of Solid-State Circuits **51**(11).

Cyrysa, J., G. Dietrich, W. Kreyling, T. Tuch and J. Heinrich (2001). "PM2.5 measurements in ambient aerosol: comparison 2.5 between Harvard impactor (HI) and the tapered element oscillating microbalance (TEOM) system." The Science of the Total Environment **278**: 191-197.

Health, N. I. f. O. S. a. (2010). "Best Practices for Dust Control in Coal Mining. IC 9517 INFORMATION CIRCULAR." DEPARTMENT OF HEALTH AND HUMAN SERVICES Centers for Disease Control and Prevention National Institute for Occupational Safety and Health Office of Mine Safety and Health Research Pittsburgh, PA, Spokane, WA.

Hinds, W. C. (1999). Aerosol technology - properties, behavior, and measurement of airborne particles. New York, Wiley-Interscience.

Rupprecht, E., M. Meyer and H. Patashuick (1992). "The Tapered Element Oscillating Microbalance As A Tool For Measuring Ambient Particulate Concentrations In Real Time." J. Aerosol Sci. **23**(1): S635-S638.

Schindelin, J., I. Arganda-Carreras, E. Frise, V. Kaynig, M. Longair, T. Pietzsch, S. Preibisch, C. Rueden, S. Saalfeld and B. Schmid (2012). "Fiji: an open-source platform for biological-image analysis." Nature methods **9**(7): 676-682.

Su, W.-C. and J. H. Vincent (2004). "Experimental Measurements and Numerical Calculations of Aspiration Efficiency for Cylindrical Thin-Walled Aerosol Samplers in Perfectly Calm Air." Aerosol Sci. Technol. **38**(8).

Systems, D. (2017). "ProX SLS 500." Retrieved from: https://www.3dsystems.com/3d-printers/prox-sls-500.

Tsai, C. and D. Theisen (2018). "A Sampler Designed for Nanoparticles and Respirable Particles with Direct Analysis Feature." J Nanopart Res **20**(209).

Zarringhalam, H., N. Hopkinson, N. F. Kamperman and J. J. De Vlieger (2006). "Effects of processing on microstructure and properties of SLS Nylon 12." Materials Science and Engineering **A**(435).